Title
Circadian control of tumor immunosuppression affects efficacy of immune checkpoint blockade

Journal
Nature Immunology, 25(7)

ISSN
1529-2908

Authors
Fortin, Bridget M
Pfeiffer, Shannon M
Insua-Rodríguez, Jacob
et al.

Publication Date
2024-07-01

DOI
10.1038/s41590-024-01859-0

nature immunology

Article

https://doi.org/10.1038/s41590-024-01859-0

Circadian control of tumor immunosuppression affects efficacy of immune checkpoint blockade

Received: 9 November 2023

Accepted: 29 April 2024

Published online: 28 May 2024

Check for updates

Bridget M. Fortin[1], Shannon M. Pfeiffer[1], Jacob Insua-Rodríguez[1,2], Hamad Alshetaiwi[3,4], Alexander Moshensky[2], Wei A. Song[1], Alisa L. Mahieu[1], Sung Kook Chun[1], Amber N. Lewis[1], Alex Hsu[1], Isam Adam[2], Oliver S. Eng[4,5], Nicholas R. Pannunzio[1,4,6,7], Marcus M. Seldin[1,4,7], Ivan Marazzi[1,4,7], Francesco Marangoni[2,4], Devon A. Lawson[2,4,7], Kai Kessenbrock[1,4,7] & Selma Masri[1,4,7]

The circadian clock is a critical regulator of immunity, and this circadian control of immune modulation has an essential function in host defense and tumor immunosurveillance. Here we use a single-cell RNA sequencing approach and a genetic model of colorectal cancer to identify clock-dependent changes to the immune landscape that control the abundance of immunosuppressive cells and consequent suppression of cytotoxic $CD8^+$ T cells. Of these immunosuppressive cell types, PD-L1-expressing myeloid-derived suppressor cells (MDSCs) peak in abundance in a rhythmic manner. Disruption of the epithelial cell clock regulates the secretion of cytokines that promote heightened inflammation, recruitment of neutrophils and the subsequent development of MDSCs. We also show that time-of-day anti-PD-L1 delivery is most effective when synchronized with the abundance of immunosuppressive MDSCs. Collectively, these data indicate that circadian gating of tumor immunosuppression informs the timing and efficacy of immune checkpoint inhibitors.

Colorectal cancer (CRC) is a significant health challenge globally, with high morbidity and mortality rates that are rising in young adults[1,2]. The current standard of care for CRC relies on 5-fluorouracil-based chemotherapy that lacks specificity and is associated with significant toxicity[3]. Immunotherapy has emerged as a promising approach for the treatment of multiple cancer types[4]. Although immune checkpoint inhibitors (ICIs) have demonstrated efficacy in patients with advanced, microsatellite instability high CRC[5,6], which is known for its pronounced immunogenicity, the majority of CRC cases remain unresponsive. Also, even among cancers that are highly responsive to immunotherapy, a majority of patients demonstrate disease progression on ICI therapy[7,8]. Thus, these findings represent a significant clinical hurdle in the treatment of solid tumors and underscore the need to improve the efficacy of ICIs.

The circadian clock is the biological timekeeping mechanism that governs endocrine, metabolic and immune functions to maintain physiological homeostasis[9–12]. The clock impinges on innate immunity by regulating time-of-day-dependent production and trafficking of

[1]Department of Biological Chemistry, University of California Irvine, Irvine, CA, USA. [2]Department of Physiology and Biophysics, University of California Irvine, Irvine, CA, USA. [3]Department of Pathology, University of Hail, Hail, Saudi Arabia. [4]Chao Family Comprehensive Cancer Center, University of California Irvine, Irvine, CA, USA. [5]Department of Surgery, Division of Surgical Oncology, University of California Irvine, Orange, CA, USA. [6]Department of Medicine, Division of Hematology/Oncology, University of California Irvine, Irvine, CA, USA. [7]Center for Epigenetics and Metabolism, University of California Irvine, Irvine, CA, USA. e-mail: smasri@uci.edu

https://doi.org/10.1038/s41590-024-01859-0

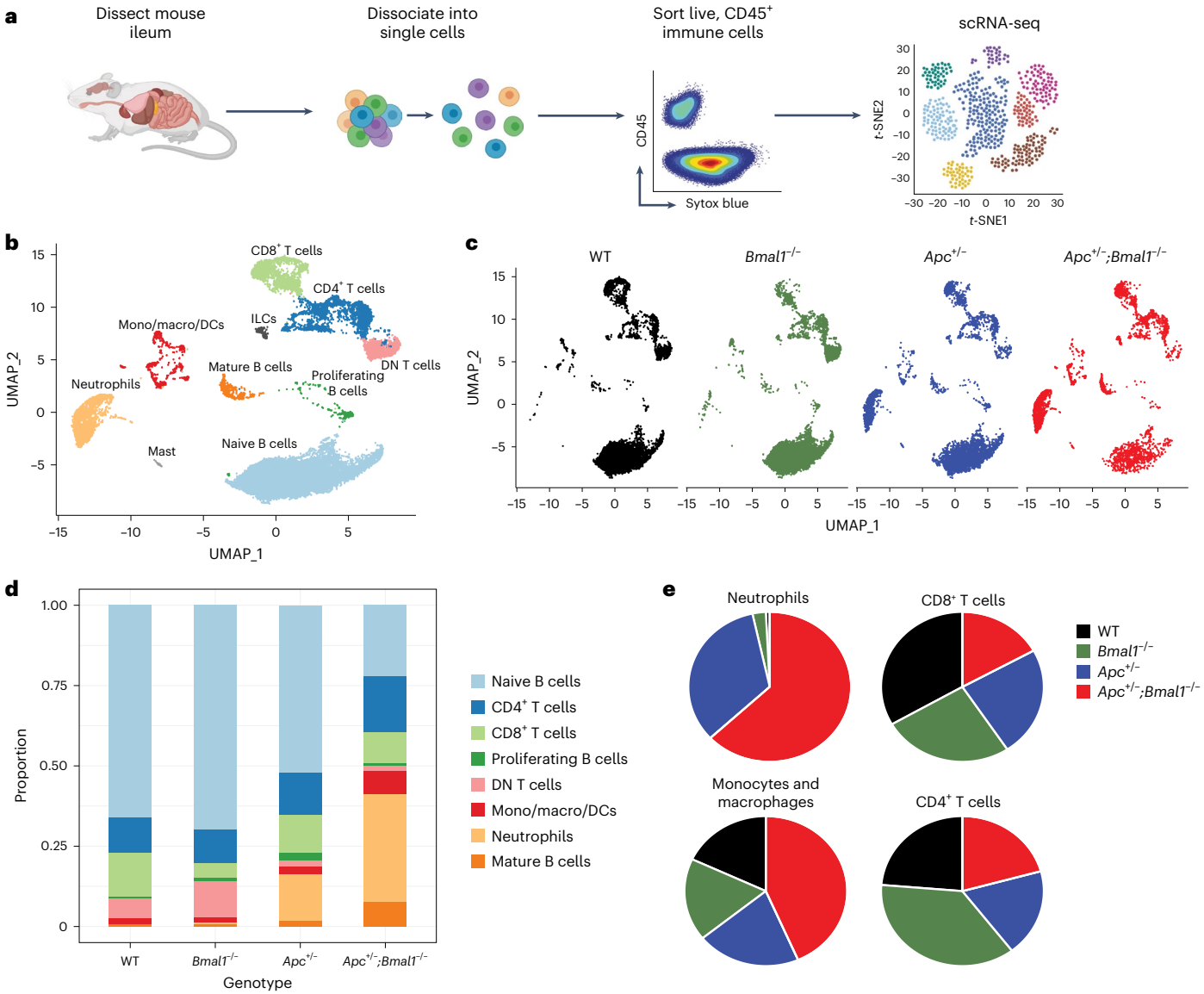

Fig. 1 | Circadian clock disruption alters the immune landscape. a, Schematic depicting the workflow for scRNA-seq of live, CD45$^+$ immune cells sorted from mouse small intestine isolated at ZT 4. **b**, UMAP of cell types clustered by single-cell transcriptional analysis ($n = 15{,}234$ cells, $n = 3$ mice per genotype). **c**, UMAP of cell types clustered by single-cell transcriptional analysis broken down by mouse genotype WT, *Bmal1*$^{-/-}$, *Apc*$^{+/-}$ and *Apc*$^{+/-}$;*Bmal1*$^{-/-}$. **d**, Immune cell composition by genotype from WT, *Bmal1*$^{-/-}$, *Apc*$^{+/-}$ and *Apc*$^{+/-}$;*Bmal1*$^{-/-}$ mice. **e**, Pie chart of neutrophils, CD8$^+$ T cells, monocytes/macrophages and CD4$^+$ T cells from WT, *Bmal1*$^{-/-}$, *Apc*$^{+/-}$ and *Apc*$^{+/-}$;*Bmal1*$^{-/-}$ mice.

cytokines/chemokines, as well as immune cell maturation and tissue infiltration[13–16]. In particular, myeloid cell-specific deletion of *Bmal1* was shown to abrogate the rhythmic cycling of monocytes and promote the accumulation of inflammatory Ly6C^{hi} monocytes in non-tumor models[17,18]. While these studies establish a causal link between the circadian clock and innate immunity, less is known regarding how the clock impacts antitumor immunity. Using an MMTV:PyMT breast cancer model and xenograft model of melanoma, the abundance and function of tumor-antigen-specific CD8$^+$ T cells was found to be clock-controlled and regulated by dendritic cells (DCs)[19,20]; however, whether the activity of cytotoxic CD8$^+$ T cells is also dependent on clock-controlled regulation of immunosuppression remains mechanistically undefined.

Chronomedicine suggests that the timing of delivery of cancer therapeutics can significantly impact treatment outcome. In support of this, studies have provided compelling evidence that morning administration of chemotherapy can mitigate side effects and enhance treatment response across diverse cancer types[21–23]. Preclinical models and early-stage clinical trials have also demonstrated increased efficacy of cytokine infusions in a time-of-day-dependent manner[24–26]. In terms of delivery timing of ICIs, studies are limited with the exception of retrospective analyses of multiple tumor types, where afternoon dosing of ICIs was significantly associated with shorter overall survival[27–30]. Notably, immunotherapy agents exhibit rapid, partial tissue-clearance within 12 h after administration[31], indicating that the timing of treatment could be critical for stimulating antitumor immunity.

Here, we show that the circadian clock impinges on tumor immunosuppression to control optimal timing of ICI therapy. Using a genetic model of CRC and a single-cell RNA sequencing (scRNA-seq) approach we identify clock-dependent control of the immune landscape within the tumor microenvironment. Genetic and environmental disruption of the circadian clock resulted in accumulation of MDSCs and a decrease in the number of cytotoxic CD8$^+$ T cells. More specifically, we identified an important signaling axis between the intestinal epithelial circadian clock and immune cells through the secretion of pro-inflammatory

cytokines and chemokines. Given the role of the circadian network in regulating immunity, the abundance of PD-L1-expressing MDSCs was found to be rhythmic in the intestine and in peripheral tissues. We also show that anti-PD-L1 administration is most effective in the early active phase of mice when immunosuppressive MDSCs are more abundant. These results demonstrate that clock-dependent control of antitumor immunity can inform the optimal timing and efficacy of the immune checkpoint blockade.

Results

Clock disruption alters the immune landscape

A growing body of evidence suggests a critical link between circadian clock dysregulation and multiple different types of cancer[19,32–43]. We previously reported that clock disruption promotes tumor progression in an *Apc*-driven model of CRC[39]. Our genetically engineered mouse model (GEMM) harbors both intestine-specific knockout of *Bmal1*, to disrupt the clock and heterozygous deletion of *Apc*, to initiate CRC (Extended Data Fig. 1a,b). *Apc* and *Bmal1* were selectively deleted in intestinal epithelial cells (*Apc*$^{+/\Delta ex1\text{-}15}$*;Bmal1*$^{fl/fl}$*;Villin-Cre)* using Villin-Cre, and we denote *Bmal1*$^{fl/fl}$*;Villin-Cre* mice as *Bmal1*$^{-/-}$, *Apc*$^{+/\Delta ex1\text{-}15}$*;Villin-Cre* mice as *Apc*$^{+/-}$, and *Apc*$^{+/\Delta ex1\text{-}15}$*;Bmal1*$^{fl/fl}$*;Villin-Cre* mice as *Apc*$^{+/-}$*;Bmal1*$^{-/-}$. Of note, in the *Bmal1*$^{-/-}$ and *Apc*$^{+/-}$*;Bmal1*$^{-/-}$ mice, the clock is only disrupted in intestinal epithelial cells and remains intact in the periphery, thus establishing a system to delineate the crosstalk between the intestinal epithelial clock and the immune system. Furthermore, defining this axis is critical for advancing our understanding of time-of-day control of antitumor immunity.

Using this GEMM of CRC, we previously reported the impact of clock disruption on tumor burden and pathological features[39]. Intestinal hematoxylin and eosin (H&E)-stained sections from *Apc*$^{+/-}$ mice contained early neoplastic precursor lesions and tubular adenomas[39]. In contrast, *Apc*$^{+/-}$*;Bmal1*$^{-/-}$ mice showed a striking increase in neoplastic changes, ranging from tubular adenomas to locally invasive adenocarcinomas extending into the muscularis propria[39]. Additionally, polyp count, which includes early neoplastic precursor lesions, tubular adenomas and locally invasive adenocarcinomas, was used to quantify tumor burden. *Apc*$^{+/-}$*;Bmal1*$^{-/-}$ mice were found to have significantly greater intestinal polyp count versus *Apc*$^{+/-}$ mice (Extended Data Fig. 1c). Spleen weight was also significantly elevated in *Apc*$^{+/-}$*;Bmal1*$^{-/-}$ mice compared to *Apc*$^{+/-}$ mice (Extended Data Fig. 1d), suggesting increased systemic inflammation in clock mutant, tumor-bearing mice. Together, these data link disruption of the circadian clock in the intestine to acceleration of CRC progression.

The circadian clock has been linked with immunity through time-of-day-dependent regulation of cytokine/chemokine production, as well as the release and trafficking of immune cells to target tissues[13,14,16,43,44]; however, how circadian clock disruption in intestinal epithelial cells regulates tissue-specific and systemic control of antitumor immunity is unknown. Therefore, to define the impact of clock disruption on the immune landscape in the intestine, we performed scRNA-seq with CD45$^+$ sorted immune cells isolated at Zeitgeber time (ZT) 4 from wild-type (WT), *Bmal1*$^{-/-}$, *Apc*$^{+/-}$ and *Apc*$^{+/-}$*;Bmal1*$^{-/-}$ mice (Fig. 1a). Based on Uniform Manifold Approximation and Projection (UMAP) clustering and analyses of immune cell lineage marker expression (Extended Data Figs. 1e,f and 2a), scRNA-seq identified distinct clusters of myeloid and lymphoid cells. These cells included neutrophils (*S100a8*, *S100a9* and *Cxcr2*), monocytes/macrophages/dendritic cells (DCs) (*C1qa*, *C1qb* and *Fn1*), mast cells (*Kit*), CD8$^+$ T cells (*CD8a*, *Gzma* and *Ccl5*), CD4$^+$ T cells (*CD4*, *Ms4a4b* and *Trbc2*), double-negative (DN) T cells (*Ms4a4b*, *Trbc2*, low for *CD4* and *CD8a*), innate lymphoid cells (*Il7r*, *Gata3* and *Klrg1*), naive B cells (*CD19*, *Ms4a1* and *CD79a*), mature B cells (*Jchain*, *Igha* and *Igkc*) and proliferating B cells (*Mki67*, *Top2a* and *Pclaf*) (Fig. 1b). Immune cell populations that were clock-dependent or tumor-specific were analyzed further. Notably, scRNA-seq revealed differences in the immune landscape in the *Bmal1*$^{-/-}$, *Apc*$^{+/-}$ and *Apc*$^{+/-}$*;Bmal1*$^{-/-}$ mice compared to WT (Fig. 1b–e). Of note, clock disruption alone, in the absence of cancer initiation, also altered the immune landscape. When compared to WT, *Bmal1*$^{-/-}$, *Apc*$^{+/-}$ and *Apc*$^{+/-}$*;Bmal1*$^{-/-}$ mice had increased proportions of neutrophils as well as decreased proportions of CD8$^+$ T cells, with less of an impact on monocytes/macrophages, DCs, B cells, CD4$^+$ T cells and CD25$^+$ T cells (Fig. 1d,e and Extended Data Fig. 2b–d). Based on total numbers of myeloid and lymphoid cells, the most striking difference was an increase in the number of neutrophils in the *Bmal1*$^{-/-}$, *Apc*$^{+/-}$ and *Apc*$^{+/-}$*;Bmal1*$^{-/-}$ mice (Fig. 1d,e and Extended Data Fig. 2c). This increase in neutrophils in the clock-disrupted mice suggests that neutrophils could be a potential driver of these immune alterations.

Also, multiple B cell clusters were identified in the scRNA-seq data, including naive B cells, mature B cells and proliferating B cells (Fig. 1d and Extended Data Fig. 2d,e), consistent with the literature differentiating these B cell subtypes[45]. Notably, the count of naive B cells decreased, whereas mature B cells increased only in the tumor-bearing *Apc*$^{+/-}$ and *Apc*$^{+/-}$*;Bmal1*$^{-/-}$ mice, and this was independent of clock disruption (Fig. 1d and Extended Data Fig. 2d,e). Based on published reports, cancer development promotes tumor infiltration of B cells that alters their cell surface marker expression, identity and function, thus resulting in increased B cell heterogeneity[46,47]. These findings are consistent with our scRNA-seq data illustrating a tumor-specific role for remodeling of B cells.

Clock disruption promotes immune microenvironment remodeling

To further define changes to the immune landscape following clock disruption, a flow cytometry panel was established to quantify immune cell types within the intestine and spleen (Extended Data Fig. 3a). Both panels included a marker to gate live cells as well as CD45 for sorting bulk immune cells. The myeloid panel included CD11b for myeloid cells, F4/80 for macrophages, Ly6C for monocytes and Ly6G for neutrophils. The lymphocyte panel included CD3 for T cells, CD4 for CD4$^+$ T cells, CD8 for CD8$^+$ T cells and CD25 for CD25$^+$ T cells. These mice were separated to profile the impact of the clock in the absence (WT and *Bmal1*$^{-/-}$) and presence (*Apc*$^{+/-}$ and *Apc*$^{+/-}$*;Bmal1*$^{-/-}$) of a tumor microenvironment, as we expect greater immune cell changes during cancer progression. Notably, clock disruption did not alter the total frequency of intestinal CD45$^+$ immune cells (Extended Data Fig. 4a). Both *Bmal1*$^{-/-}$ and *Apc*$^{+/-}$*;Bmal1*$^{-/-}$ mice had significantly higher proportions

Fig. 2 | Genetic and environmental clock disruption alter the immune landscape. a, Neutrophils, monocytes, macrophages, and CD8$^+$ T cells shown as percent of CD45$^+$ cells from the small intestine of WT and *Bmal1*$^{-/-}$ mice killed at ZT 4 and analyzed by flow cytometry ($n = 7$ mice per genotype). **b**, Neutrophils, monocytes, macrophages and CD8$^+$ T cells shown as percent of CD45$^+$ cells from the small intestine of *Apc*$^{+/-}$ and *Apc*$^{+/-}$*;Bmal1*$^{-/-}$ mice killed at ZT 4 and analyzed by flow cytometry ($n = 7$ mice per genotype). **c**, Schematic of environmental SD paradigm in WT mice performed for 8 weeks. Light versus dark schedule is shown for 5 days. **d**, Neutrophils, monocytes, macrophages and CD8$^+$ T cells shown as percent of CD45$^+$ cells from the small intestine of WT mice subjected to 12-h LD versus SD paradigm. Mice were killed at ZT 4 and analyzed by flow cytometry ($n = 8$ mice per genotype). **e**, Representative proportions of neutrophils and monocytes in the small intestine of WT mice subjected to the 12-h LD paradigm versus 1 week SD, 3 weeks SD and 5 weeks SD. **f**, Neutrophils, monocytes, macrophages and CD8$^+$ T cells shown as percent of CD45$^+$ cells from the small intestine of WT mice subjected to the 12-h LD paradigm versus 1 week SD, 3 weeks SD and 5 weeks SD. Mice were killed at ZT 4 and analyzed by flow cytometry ($n = 6$ mice per genotype). Data represent mean ± s.e.m. and statistical significance was determined by two-tailed Mann–Whitney *T*-test (**a**,**b**,**d**) and one-way analysis of variance (ANOVA) with Tukey's multiple comparison test (**f**). $^*P < 0.05$; $^{**}P < 0.01$; $^{***}P < 0.001$; NS, not significant.

https://doi.org/10.1038/s41590-024-01859-0

of neutrophils and monocytes, as well as significantly reduced proportions of CD8$^+$ T cells (Fig. 2a,b and Extended Data Fig. 4b–e). Of these changes, the increase in neutrophils was the most prominent, with a fivefold increase in the *Bmal1*$^{-/-}$ intestine compared to WT and a fivefold increase in the *Apc*$^{+/-}$;*Bmal1*$^{-/-}$ intestine compared to *Apc*$^{+/-}$ (Fig. 2a,b). This suggests that clock disruption promotes an increase in neutrophils in both non-tumor-bearing and tumor-bearing microenvironments. The proportions of total CD3$^+$ T cells, CD4$^+$ T cells and CD25$^+$ T cells in the intestine were unaffected by clock disruption (Extended Data Fig. 5a). Spleens isolated from *Bmal1*$^{-/-}$ and *Apc*$^{+/-}$;*Bmal1*$^{-/-}$ mice

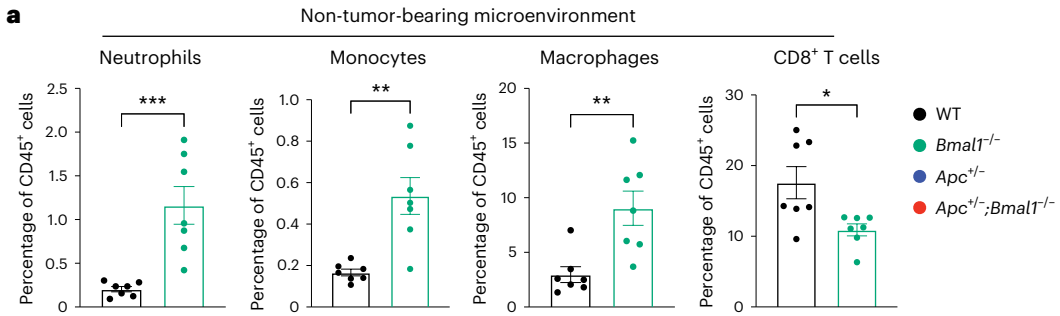

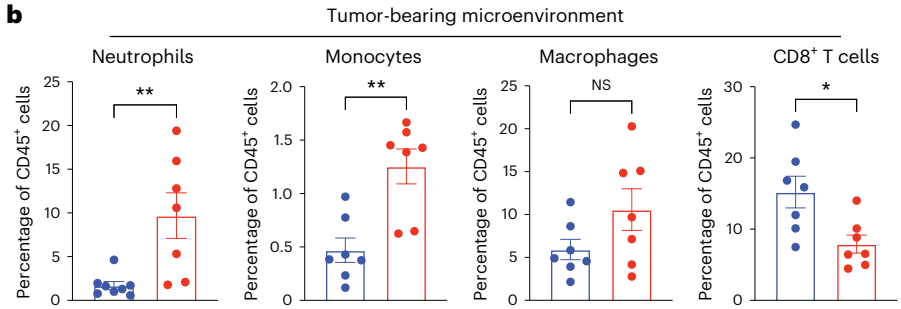

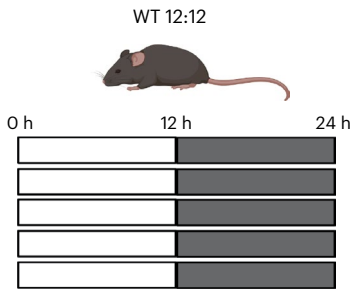

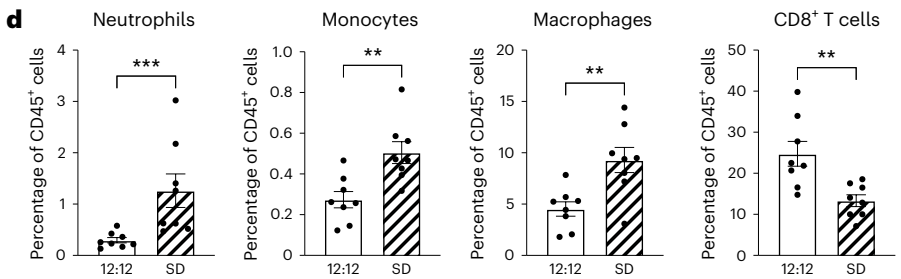

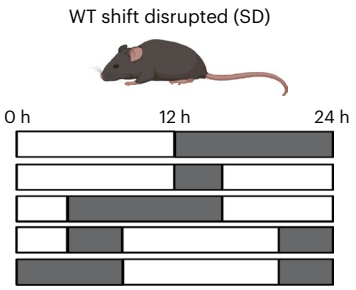

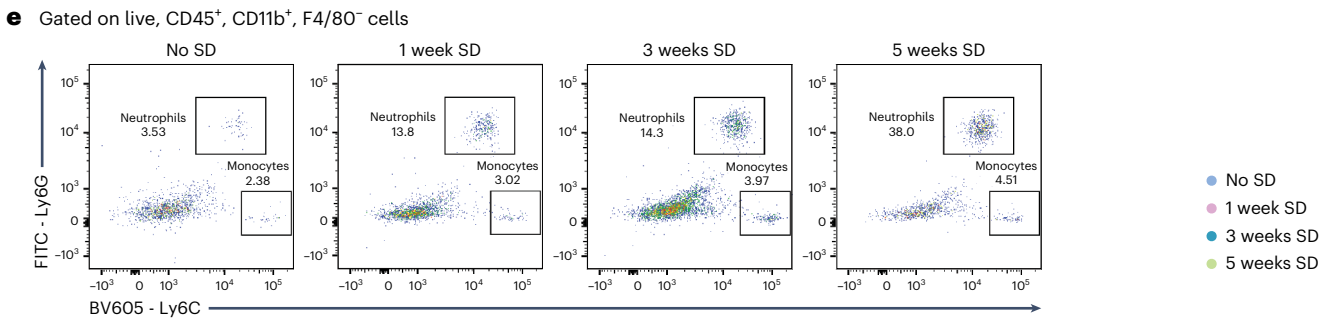

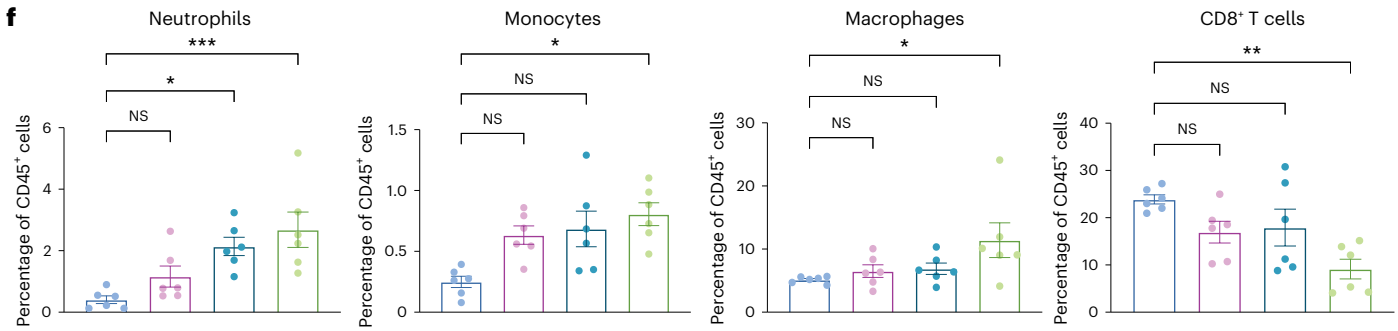

also had significantly higher proportions of neutrophils and monocytes (Extended Data Fig. 5b). We also profiled the abundance of macrophages and CD25$^+$ T cells in both the intestine and spleen and did not observe a consistent clock-dependent effect (Fig. 2a,b and Extended Data Fig. 5a,b). These flow cytometry data suggest that clock disruption in intestinal epithelial cells significantly increased the abundance of neutrophils in tumor-bearing and non-tumor-bearing mice, which is corroborated by our scRNA-seq analysis.

In humans, circadian rhythms are frequently disrupted by environmental stimuli, including night shift work, jet lag and extended light-at-night exposure[48], and several of these environmental disruption paradigms have been shown to accelerate cancer progression in mice[19,32,33,35,36,39,49]. Therefore, to define whether environmental clock disruption mirrors the alterations to the immune landscape seen with genetic clock disruption, WT mice were exposed to an established environmental shift paradigm that models jet lag and night shift work 3–4 times per week for 8 weeks (Fig. 2c)[19,36,39]. We previously used this paradigm and demonstrated a significant loss of rhythmicity of the respiratory exchange ratio, locomotor activity and food intake, signifying a systemic disruption of the circadian clock[39]. Shift disruption (SD) significantly increased proportions of neutrophils, monocytes and macrophages, and resulted in a significant reduction in CD8$^+$ T cells in the intestine (Fig. 2d). Neither genetic clock disruption alone (Extended Data Fig. 1d) nor environmental clock disruption (Extended Data Fig. 5c) led to an increase in the spleen weight that is seen in the tumor-bearing mice (Extended Data Fig. 1d). This suggests that tumor progression is necessary for spleen enlargement. Last, SD led to a significant reduction in the proportion of CD4$^+$ T cells (Extended Data Fig. 5d), likely because environmental clock disruption impacts rhythmicity in both intestinal epithelial cells and immune cells systemically. Taken together, data from our environmental paradigm corroborate findings from the genetic clock mutant model and demonstrate that clock disruption alters immune cell frequency, both systemically and locally within the intestine.

Of note, genetic and environmental clock disruption were found to alter proportions of both myeloid and lymphoid cells (Fig. 2a–d). To determine which cell type was initially impacted by circadian clock disruption, WT mice were exposed to an SD time-course for 1 week, 3 weeks or 5 weeks and flow cytometry was subsequently used to track changes to the immune landscape. Similar to mice exposed to 8 weeks of the SD paradigm (Extended Data Fig. 5c), spleen weight was unaffected by short-term SD exposure (Extended Data Fig. 5e); however, SD led to a significant increase in the proportion of neutrophils after only 3 weeks (Fig. 2e,f). This was followed by an increase in the proportion of monocytes and macrophages and a reduction in the proportion of CD8$^+$ T cells after 5 weeks of environmental shift (Fig. 2f). The proportion of CD4$^+$ T cells was unaffected after 5 weeks of SD (Extended Data Fig. 5f) and reduced only after 8 weeks of shift (Extended Data Fig. 5d), demonstrating that abundance of CD4$^+$ T cells is not initially changed following circadian clock disruption. These data suggest that environmental clock disruption triggers an initial alteration in neutrophil proportions before secondary immune cell adaptations, including a reduction in cytotoxic CD8$^+$ T cells.

Disruption of the clock promotes MDSC accumulation

Our data suggest that clock disruption plays an important role in regulating immune cell proportions in CRC, yet how this influences cancer progression remains undefined. Notably, genetic knockout of *Bmal1* alone resulted in a pronounced decrease in intestinal cytotoxic CD8$^+$ T cells (Figs. 1d,e and 2a), suggesting that the circadian clock is involved in immunosuppression. Our scRNA-seq identified a cluster of myeloid cells (mainly neutrophils) that highly expressed markers of MDSCs, including *Ifitm1*, *Wfdc17*, *S100a8*, *S100a9*, *Irg1* and *Arg2* (Extended Data Fig. 6a). This neutrophilic population is enriched as a result of both clock disruption and cancer (Extended Data Fig. 6b). MDSCs, often neutrophil- and monocyte-derived, have been reported to suppress cytotoxic CD8$^+$ T cell proliferation and activity[50,51] and recent evidence suggests that increased accumulation of neutrophils can induce immunosuppression and tumor progression[20,52,53].

To further define this, putative MDSCs were sorted by flow cytometry from the intestines and spleens of WT, *Bmal1*$^{-/-}$, *Apc*$^{+/-}$ and *Apc*$^{+/-}$;*Bmal1*$^{-/-}$ mice (Fig. 3a and Extended Data Fig. 3b). Of note, these mice were separated to profile the impact of clock disruption in non-tumor-bearing versus tumor-bearing microenvironments. MDSCs consist of two major subsets of Ly6G$^+$Ly6C^{low} granulocytic and Ly6G$^-$Ly6C^{high} monocytic cells[54,55]. Thus, CD11b, a marker for myeloid cells, and Gr1, a marker for both Ly6C and Ly6G, were used to sort both monocytes and neutrophils, the most common populations comprising MDSCs[54,55]. Both *Bmal1*$^{-/-}$ and *Apc*$^{+/-}$;*Bmal1*$^{-/-}$ mice had significantly greater proportions of Gr1$^+$ cells (Fig. 3b–d). MDSCs can suppress T cells through the generation of reactive oxygen species (ROS)[50]. To determine if the production of ROS is influenced by clock disruption, we used cell permeable reagent 2′,7′-dichlorofluorescin diacetate (H_2DCFDA), which becomes fluorescent DCF in the presence of ROS, to quantitatively measure ROS accumulation in the mouse intestine. Gr1$^+$ cells from *Bmal1*$^{-/-}$ and *Apc*$^{+/-}$;*Bmal1*$^{-/-}$ mice exhibited greater levels of ROS (Fig. 3e,f). An additional mechanism of T cell suppression is the upregulation of PD-L1 by MDSCs[56,57]. A greater percentage of Gr1$^+$ cells from *Bmal1*$^{-/-}$ and *Apc*$^{+/-}$;*Bmal1*$^{-/-}$ mice were also found to be PD-L1$^+$ (Fig. 3g,h), suggesting these MDSCs could be immunosuppressive. Similarly, gene expression analysis of splenic Gr1$^+$ cells revealed a significant upregulation of immunosuppressive genes, including *S100a8*, *S100a9* and *Wfdc17* in the *Bmal1*$^{-/-}$ and *Apc*$^{+/-}$;*Bmal1*$^{-/-}$ mice (Fig. 3i,j). All primer sequences can be found in Table 1. These data demonstrate that clock disruption, even in the absence of a tumor microenvironment, promotes the accumulation of immunosuppressive myeloid cells.

To confirm the immunosuppressive ability of these putative MDSCs at the functional level, a classical T cell suppression assay was performed. This assay involved activating naive T cells with CD3/CD28 and staining with a proliferation dye eFluor670 that is diluted as a result of consecutive cell divisions. Next, activated T cells were co-cultured with Gr1$^+$ cells isolated from WT, *Bmal1*$^{-/-}$, *Apc*$^{+/-}$ and *Apc*$^{+/-}$;*Bmal1*$^{-/-}$ mice. After 3 days of co-culture, flow cytometry was used to measure the counts of CD4$^+$ and CD8$^+$ T cells as well as the proportion of these cells that maintained the proliferation dye, allowing for a quantification

Fig. 3 | Disruption of the circadian clock promotes the accumulation of MDSCs. a, Schematic depicting workflow for MDSC assays including T cell co-culture and proliferation, ROS quantification and MDSC qPCR from live, CD45$^+$CD11b$^+$Gr1$^+$ sorted cells. **b**, Representative percent of Gr1$^+$ cells after gating for live, CD45$^+$CD11b$^+$ cells from WT, *Bmal1*$^{-/-}$, *Apc*$^{+/-}$ and *Apc*$^{+/-}$;*Bmal1*$^{-/-}$ small intestine using flow cytometry. **c**,**d**, Quantification of Gr1$^+$ cells as percent of CD45$^+$ cells from the small intestine of WT, *Bmal1*$^{-/-}$, *Apc*$^{+/-}$ and *Apc*$^{+/-}$;*Bmal1*$^{-/-}$ mice killed at ZT 4 and analyzed by flow cytometry ($n = 3$ mice per genotype). **e**,**f**, Geometric mean of DCF from the small intestine of WT, *Bmal1*$^{-/-}$, *Apc*$^{+/-}$ and *Apc*$^{+/-}$;*Bmal1*$^{-/-}$ mice killed at ZT 4 and analyzed by flow cytometry ($n = 4$ mice per genotype). **g**,**h**, Gr1$^+$PD-L1$^+$ cells shown as percent of CD45$^+$ cells from the small intestine of WT, *Bmal1*$^{-/-}$, *Apc*$^{+/-}$ and *Apc*$^{+/-}$;*Bmal1*$^{-/-}$ mice killed at ZT 4 and analyzed by flow cytometry ($n = 3$ mice per genotype). **i**,**j**, Expression of *s100a8, s100a9* and *Wfdc17* as determined by qPCR using splenic Gr1$^+$ sorted cells from WT, *Bmal1*$^{-/-}$, *Apc*$^{+/-}$ and *Apc*$^{+/-}$;*Bmal1*$^{-/-}$ mice killed at ZT 4 ($n = 3$ mice per genotype). **k**, Bar graph of CD4$^+$ and CD8$^+$ T cell counts measured by FACS quantification in inactivated T cells or CD3/CD28 activated T cells with a 1:1 ratio of CD11b$^+$Gr1$^+$ cells from WT, *Bmal1*$^{-/-}$, *Apc*$^{+/-}$ and *Apc*$^{+/-}$;*Bmal1*$^{-/-}$ spleen ($n = 3$ mice per genotype). Data represent mean ± s.e.m. Statistical significance was determined by two-tailed Mann–Whitney *T*-test (**c**–**j**) and one-way ANOVA with Tukey's multiple comparison (**k**). *$P < 0.05$; **$P < 0.01$; ***$P < 0.001$; ****$P < 0.0001$; NS, not significant.

https://doi.org/10.1038/s41590-024-01859-0

of T cell proliferation and a readout for immunosuppression (Extended Data Fig. 3c). We found that MDSCs from clock-disrupted *Bmal1*$^{-/-}$ and tumor-bearing *Apc*$^{+/-}$ and *Apc*$^{+/-}$;*Bmal1*$^{-/-}$ mice, significantly suppressed T cell proliferation (Fig. 3k and Extended Data Fig. 6c,d). Our findings suggest that immunosuppression is likely mediated through clock-dependent control of MDSCs in a model of CRC.

Clock disruption drives a Wnt-mediated inflammatory response

To define the underlying molecular mechanism of immune cell remodeling, we further dissected the role of the circadian clock in the intestinal epithelium. Wnt signaling regulates development, proliferation and stemness and is an essential pathway for maintaining homeostasis in

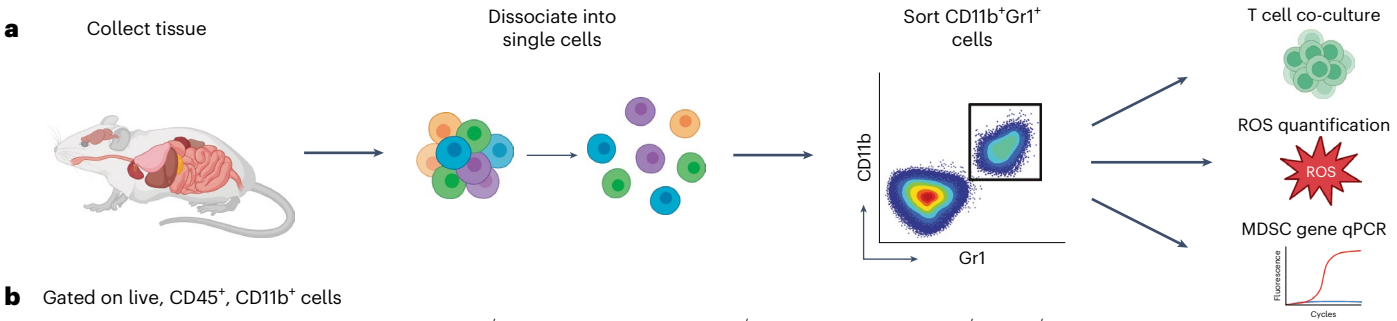

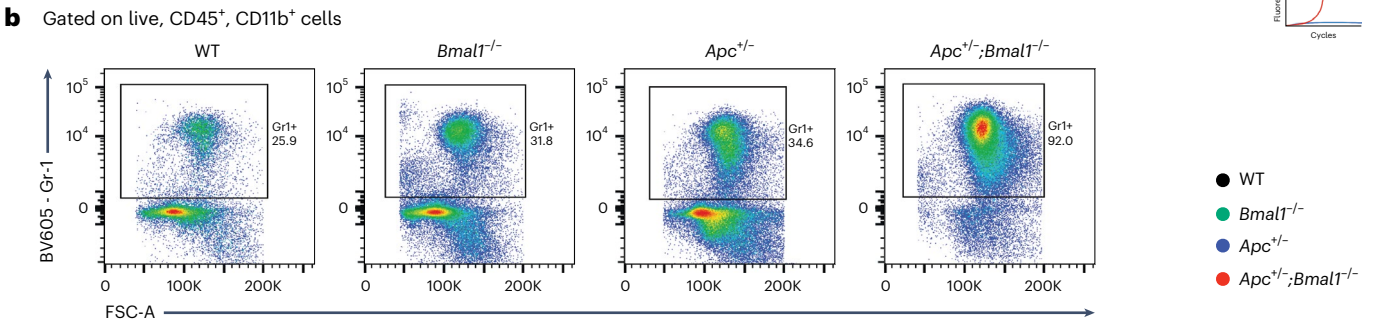

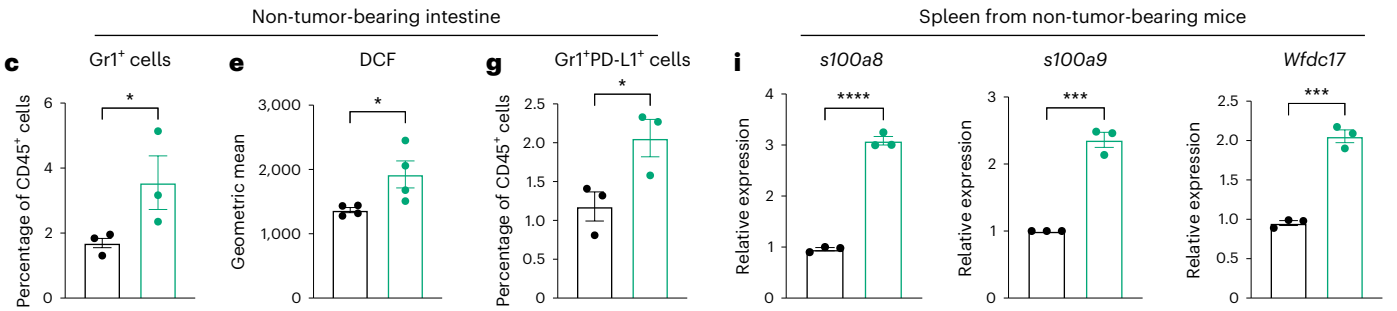

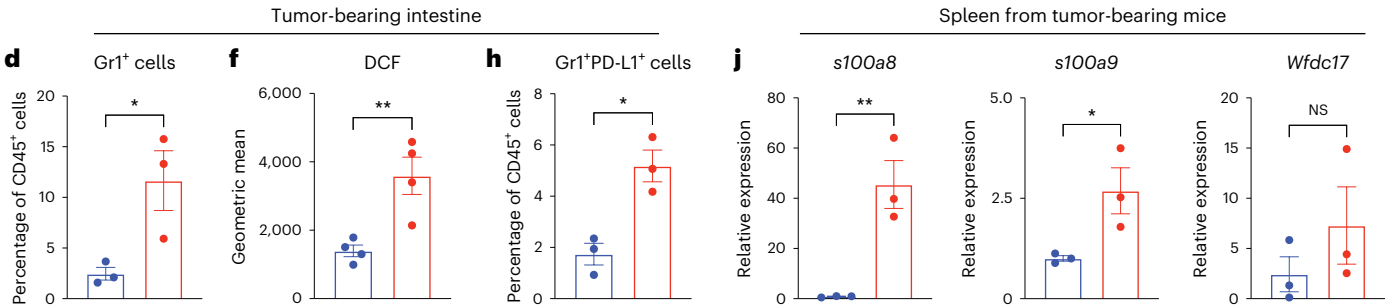

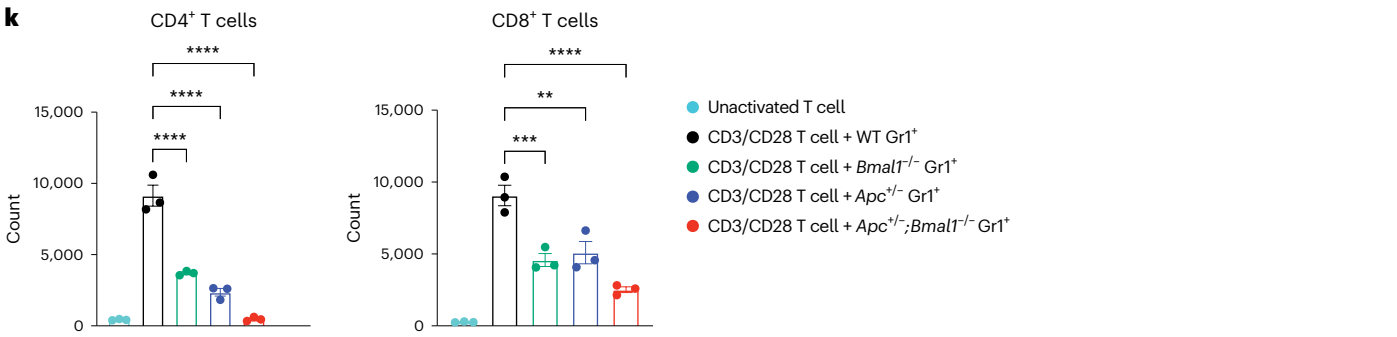

https://doi.org/10.1038/s41590-024-01859-0

Table 1 | Primers used for gene expression analysis

Mouse qPCR primer name	Primer sequence (5′ to 3′)
18S mRNA fwd	CGCCGCTAGAGGTGAAATTC
18S mRNA rev	CGAACCTCCGACTTTCGTTCT
S100a8 mRNA fwd	GTCCTCAGTTTGTGCAGAATATAAA
S100a8 mRNA rev	TTTGTGAGATGCCACACCCA
S100a9 mRNA for	TGGCAACCTTTATGAAGAAAGAGAA
S100a9 mRNA rev	GCCATCAGCATCATACACTCC
Wfdc17 mRNA for	TTTGATCACTGTGGGGATG
Wfdc17 mRNA rev	ACACTTTCTGGTGAAGGCTTG
Arg2 mRNA for	AGGAGTGGAATATGGTCCAGC
Arg2 mRNA rev	AGGGATCATCTTGTGGGACATT
c-Myc mRNA for	AGCTCGCCCAAATCCTGTAC
c-Myc mRNA rev	TTGTGCTGGTGAGTGGAGAC
Survivin mRNA for	GAACCCGATGACAACCCGAT
Survivin mRNA rev	TTGGCTCTCTCTGTCTGTCCAG
Cxcl5 mRNA for	GAGCTGCGTTGTGTTTGCTT
Cxcl5 mRNA rev	TAGCTTTCTTTTTGTCACTGCCC
Cxcl1 mRNA for	CCAGACTTGAAGGTGTTGC
Cxcl1 mRNA rev	TCTGAACCAAGGGAGCTTCA
M-csf mRNA for	AGTGGAAGTGGAGGAGCCAT
M-csf mRNA rev	TGGTGAGGGGTCATAGAATCC
Gm-csf mRNA for	GGCCTTGGAAGCATGTAGAG
Gm-csf mRNA rev	CCGTAGACCCTGCTCGAATA
Axin2 mRNA for	TGTCCTGGGGGAACAGATTA
Axin2 mRNA rev	TTTTGGCAAGGTACCACCTC

the intestine[58]. We have previously shown that *Bmal1* loss promotes *Apc* loss of heterozygosity by increasing genome instability and resulting in hyperactivation of Wnt signaling[39]. A key Wnt target gene, *c-Myc*, has also been shown to regulate inflammation and immunosuppression within the tumor microenvironment[59,60]. Taken together, these findings suggest that the circadian clock and Wnt signaling could converge to regulate inflammation and subsequent remodeling of the intestinal immune landscape.

To test this, the primary intestinal epithelium was isolated from mice and plated to establish monolayer cultures as well as routinely used intestinal organoid models, both of which recapitulate the cell identity found in the intestine[61]. WT and *Bmal1*$^{-/-}$ intestinal monolayers and organoids were treated with recombinant mouse Wnt3a to define the Wnt-dependent transcriptional response in the absence and presence of a functional clock. Intestinal *Bmal1*$^{-/-}$ led to an upregulation of MYC protein, which was further heightened in the presence of Wnt3a treatment (Fig. 4a and Extended Data Fig. 7a). Compared to WT, Wnt target genes *c-Myc* and *Survivin* were significantly upregulated in *Bmal1*$^{-/-}$ intestinal monolayers in a Wnt3a-dependent manner (Fig. 4b). Similar results were obtained using WT and *Bmal1*$^{-/-}$ intestinal organoids treated with either recombinant mouse Wnt3a or Wnt3a conditioned medium (CM) (Extended Data Fig. 7b,c). Notably, the inflammatory cytokine *Cxcl5* was also upregulated in a Wnt-dependent manner and this response was significantly enhanced upon intestinal clock disruption (Fig. 4b and Extended Data Fig. 7b,c). Together, these data highlight a potential role for Wnt signaling and the circadian clock in regulating inflammation. Therefore, we propose that clock disruption and Wnt signaling coordinately promote a heightened pro-inflammatory response to recruit myeloid cells, including neutrophils, within the intestinal epithelium (Fig. 4c).

To delineate the pro-inflammatory roles of the clock and Wnt signaling, WT and *Bmal1*$^{-/-}$ primary intestinal monolayers were treated with and without recombinant Wnt3a and a 32-plex mouse cytokine/chemokine array was performed. Notaby, both clock-dependent and Wnt-dependent increases in cytokine production were identified in both cell lysate and CM. Interleukin (IL)-5, CCL5, IL-17 and CXCL9 were found to be exclusively clock-dependent as these cytokines were significantly upregulated in *Bmal1*$^{-/-}$ intestinal monolayers compared to WT (Fig. 4d,g and Extended Data Fig. 7d). CCL5, IL-17 and CXCL9 were found to be significantly upregulated in mice during chronic intestinal inflammation and cancer, leading to the recruitment of neutrophils[62–64]. IL-17 promotes neutrophil expansion and survival as well as the production of immunosuppressive molecules *s100a8* and *s100a9* (refs. 65,66). Collectively, these data suggest that clock disruption promotes a pro-inflammatory response in intestinal epithelial cells that could drive a myeloid-dependent immunosuppressive phenotype.

In addition to clock-dependent changes in cytokine regulation, additional cytokines and chemokines were identified to be exclusively Wnt-dependent. These include CXCL1, M-CSF, G-CSF, GM-CSF, CCL2, IL-2, VEGF, TNF and IFNγ (Fig. 4e,g and Extended Data Fig. 7e), which all have pro-inflammatory roles[67]. Additionally, CXCL5, CXCL6 and CXCL2 were identified to be both clock and Wnt-dependent (Fig. 4f,g and Extended Data Fig. 8a). These cytokines are also known to be activated during an inflammatory response and consequently function as neutrophil chemoattractants[13,67–70]. To confirm our findings in an additional cell model, mouse embryonic fibroblasts were similarly treated with recombinant Wnt3a which resulted in a significant upregulation of the Wnt target genes *c-Myc*, *Survivin* and *Axin2*, as well as the inflammatory cytokines *Cxcl5*, *Cxcl1*, *M-csf* and *Gm-csf* (Extended Data Fig. 8b). Similar to intestinal organoids, *Cxcl5* was the most highly upregulated cytokine, with an over 100-fold induction in response to Wnt3a (Extended Data Fig. 8b). Finally, to define transcriptional control of inflammatory cytokines, knockdown of MYC was performed in primary intestinal monolayers. MYC knockdown resulted in a significant downregulation of *Cxcl5* gene expression (Extended Data Fig. 8c). These data suggest that MYC is at least partially involved in the Wnt-dependent transcriptional control of the pro-inflammatory cytokine *Cxcl5*.

Clock disruption promotes neutrophil migration and suppression

We identified multiple pro-inflammatory and potentially immunosuppressive cytokines that are both clock and Wnt-dependent (Fig. 4d–g); however, the functional consequence of these cytokines and chemokines on neutrophil identity, gene expression and migration remained undefined. To test this, WT and *Bmal1*$^{-/-}$ primary intestinal monolayers were treated with recombinant Wnt3a and CM was collected, to define the role of the clock and Wnt signaling on neutrophil phenotype and function. Next, naive bone marrow-derived neutrophils isolated from WT mice were incubated with CM from WT and *Bmal1*$^{-/-}$ intestinal monolayers that we have shown to secrete several pro-inflammatory cytokines and chemokines (Fig. 4d–g). Notably, only neutrophils cultured with CM collected from *Bmal1*$^{-/-}$ intestinal monolayers exhibited a Wnt-dependent upregulation of MDSC-signature genes, including *s100a8*, *s100a9*, *Wfdc17* and *Arg2* (Fig. 4h). Additionally, naive bone marrow-derived neutrophils were isolated from WT mice and placed into Transwell chambers to assess chemotaxis toward cytokine/chemokine-enriched CM. Primary neutrophils were incubated with CM from WT and *Bmal1*$^{-/-}$ intestinal monolayers and a significant proportion of neutrophils were migratory in the presence of CM from *Bmal1*$^{-/-}$ primary intestinal epithelium (Fig. 4i). These data demonstrate that clock disruption and Wnt activation promoted an immunosuppressive neutrophil phenotype as well as increased neutrophil migration.

https://doi.org/10.1038/s41590-024-01859-0

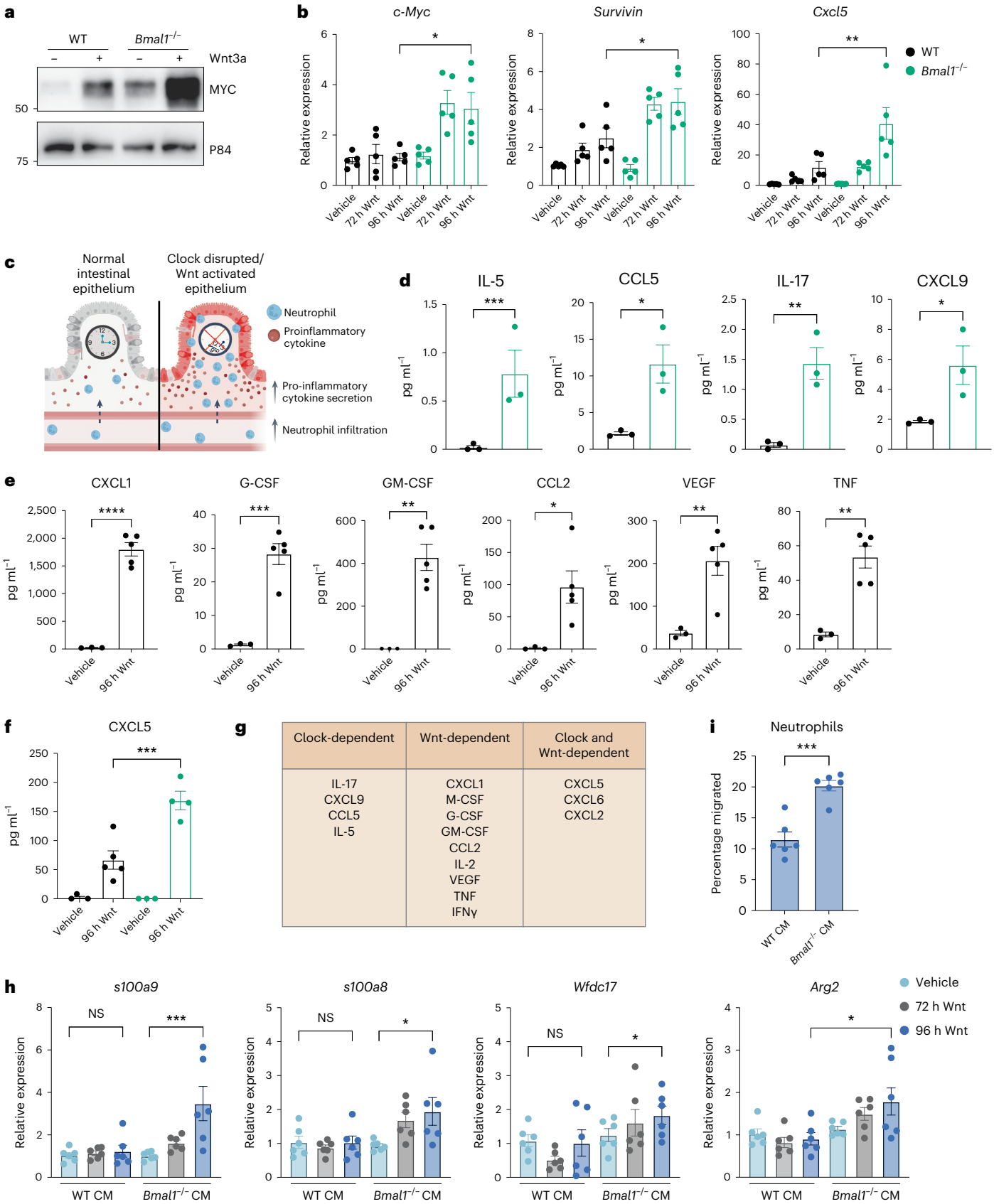

Accumulation of PD-L1^{+} myeloid cells in human CRC

To determine the physiological relevance of our findings, we analyzed the immune populations of normal human colon versus CRC tumors from 36 patients profiled by scRNA-seq[71]. We focused solely on CD45^{+} immune cells and classified naive B cells, mature B cells, T cells, NK cells and myeloid cells based on UMAP clustering and immune cell lineage marker expression (Extended Data Fig. 9a,b). We found that myeloid cells were highly abundant in human CRC samples when compared to patient-matched normal colon (Extended Data Fig. 9c,d). Notably, consistent with previous literature[72,73], PD-L1 was found to be highly

https://doi.org/10.1038/s41590-024-01859-0

Fig. 4 | Circadian clock disruption and Wnt signaling promote an inflammatory response. a, Immunoblot of MYC and p84 in WT and *Bmal1*$^{-/-}$ intestinal organoids untreated or treated with 100 ng ml^{-1} recombinant Wnt3a for 72 h. **b**, Expression of *c-Myc*, *Survivin* and *Cxcl5* determined by qPCR using WT and *Bmal1*$^{-/-}$ primary intestinal monolayers untreated or treated with 100 ng ml^{-1} recombinant Wnt3a for 72 or 96 h ($n = 5$ independent monolayer lines per genotype). **c**, Proposed model of normal versus clock-disrupted/Wnt-activated intestinal epithelium. **d**, Concentration of secreted IL-5, CCL5, IL-17 and CXCL9 in CM from WT and *Bmal1*$^{-/-}$ intestinal monolayers determined by ELISA ($n = 3$ independent monolayer lines per genotype). **e**, WT intestinal monolayers were untreated or treated with 100 ng ml^{-1} recombinant Wnt3a for 96 h ($n = 3$ untreated, $n = 5$ Wnt3a-treated independent monolayer lines per genotype). The concentration of secreted CXCL1, G-CSF, GM-CSF, CCL2, VEGF and TNF was determined by ELISA. **f**, WT and *Bmal1*$^{-/-}$ intestinal monolayers were untreated or treated with 100 ng ml^{-1} recombinant Wnt3a for 96 h ($n = 3$ untreated, $n = 4$ Wnt3a-treated independent monolayer lines per genotype). Concentration of secreted CXCL5 was determined by ELISA. **g**, Clock-dependent, Wnt-dependent and both clock- and Wnt-dependent cytokines determined by ELISA. **h**, Gene expression of *s100a9*, *s100a8*, *Wfdc17* and *Arg2* determined by qPCR of naive neutrophils cultured with WT and *Bmal1*$^{-/-}$ intestinal monolayers CM ($n = 6$ independent monolayer lines per genotype). **i**, Neutrophil migration toward WT and *Bmal1*$^{-/-}$ intestinal monolayers CM ($n = 6$ independent monolayer lines per genotype). Data represent mean ± s.e.m. Statistical significance was determined by two-tailed Mann–Whitney *T*-test (**d**,**e**,**i**) and one-way ANOVA with Tukey's multiple comparison (**b**,**f**,**h**). *$P < 0.05$; **$P < 0.01$; ***$P < 0.001$; ****$P < 0.0001$; NS, not significant.

expressed by this myeloid cluster and expression was increased in CRC samples relative to healthy colon (Extended Data Fig. 9e,f). These data suggest that PD-L1$^+$ myeloid cells are highly abundant in human CRC and this potentially immunosuppressive cell population could be therapeutically targetable.

Time-of-day anti-PD-L1 treatment affects efficacy

Utilizing our mouse scRNA-seq dataset, we assessed the expression level of PD-L1 and found that it was highly enriched in myeloid cells and specifically neutrophils (Extended Data Fig. 10a,b). Of note, the expression of PD-L1 was increased in *Bmal1*$^{-/-}$, *Apc*$^{+/-}$ and *Apc*$^{+/-}$;*Bmal1*$^{-/-}$ mice (Extended Data Fig. 10c–e). Together, these data suggest that neutrophils highly express PD-L1 and that clock disruption could be integral in driving this upregulation. Therefore, to define whether immunosuppressive MDSCs and PD-L1 expression are regulated by the circadian clock, mice were killed during the early rest phase (ZT 4) and during the early active phase (ZT 16). Flow cytometry was used to assess the proportion of Gr1$^+$ and PD-L1$^+$ cells in the intestine and peripheral tissues. Intestinal polyps and spleen weight were not significantly different between *Apc*$^{+/-}$;*Bmal1*$^{-/-}$ mice in the ZT 4 group compared to ZT 16 (Extended Data Fig. 10f,g). Of note, the circadian clock in *Apc*$^{+/-}$;*Bmal1*$^{-/-}$ mice is disrupted in intestinal epithelial cells and remains intact in other organs. In WT mice, there is a significant increase in the proportion of Gr1$^+$ and Gr1$^+$PD-L1$^+$ cells in the intestine at ZT 16 compared to ZT 4 (Fig. 5a,b). In contrast, this rhythm of Gr1$^+$ and Gr1$^+$PD-L1$^+$ cells is lost in the intestine of *Apc*$^{+/-}$;*Bmal1*$^{-/-}$ mice (Fig. 5a,b). In the spleen, where the circadian clock remains intact, we identified a significant increase in Gr1$^+$ and Gr1$^+$PD-L1$^+$ cells at ZT 16 in both WT and *Apc*$^{+/-}$;*Bmal1*$^{-/-}$ mice (Fig. 5c,d). Gr1$^+$ and Gr1$^+$PD-L1$^+$ cells were also profiled in mesenteric tumor-draining lymph node and blood, but absolute levels were low compared to the intestine and spleen (Extended Data Fig. 10h,i). We quantified cumulative levels of Gr1$^+$ and Gr1$^+$PD-L1$^+$ cells in both the intestine and spleen, the organs with the greatest proportions of these MDSCs. There were significantly more Gr1$^+$ and Gr1$^+$PD-L1$^+$ cells at ZT 16 compared to ZT 4 (Extended Data Fig. 10j,k), indicating that immunosuppressive myeloid cells peak during the early active phase. Altogether, these data demonstrate that the abundance of Gr1$^+$ MDSCs, as well as the expression of PD-L1, is rhythmic and conceptually establishes a framework for time-of-day treatment of anti-PD-L1 immunotherapy.

To assess the translational potential of our findings, *Apc*$^{+/-}$;*Bmal1*$^{-/-}$ mice were treated twice a week with anti-PD-L1 at either ZT 4 or ZT 16 for 3 weeks. We hypothesized that targeting these immunosuppressive MDSCs with anti-PD-L1 at ZT 16, when Gr1$^+$PD-L1$^+$ cells are most abundant, would provide greater antitumor efficacy. After treatment, tumor burden and spleen weight were assessed and flow cytometry was used to determine the proportions of Gr1$^+$ cells and CD8$^+$ T cells (Fig. 5e). Of note, spleen weight was increased in *Apc*$^{+/-}$;*Bmal1*$^{-/-}$ mice treated at ZT 16 and not in *Apc*$^{+/-}$;*Bmal1*$^{-/-}$ mice treated at ZT 4 (Fig. 5f), demonstrating that the inflammatory response generated by anti-PD-L1 is dependent on time-of-day delivery. Also, unlike anti-PD-L1 treatment at ZT 4, anti-PD-L1 treatment at ZT 16 significantly reduced intestinal Gr1$^+$ cells in *Apc*$^{+/-}$;*Bmal1*$^{-/-}$ mice (Fig. 5g). Treatment of *Apc*$^{+/-}$;*Bmal1*$^{-/-}$ mice with anti-PD-L1 at ZT 16 was found to promote a greater increase in intestinal CD8$^+$ T cells compared to ZT 4 treatment (Fig. 5h), suggesting a more robust antitumor immune response generated upon treatment in the early active phase. Though anti-PD-L1 treatment did not significantly decrease intestinal polyp count after only 3 weeks (Extended Data Fig. 10l), it significantly reduced polyp size in *Apc*$^{+/-}$;*Bmal1*$^{-/-}$ mice when administered at ZT 16, the time when Gr1$^+$PD-L1$^+$ cells are most abundant (Fig. 5i).

In addition to our GEMM of CRC, we also performed time-of-day anti-PD-L1 administration in subcutaneous models of CRC (MC38), lung cancer (CMT167) and melanoma (D4M-S), which are known to respond to immunotherapy[74,75]. Both ZT 4 and ZT 16 administration of anti-PD-L1 significantly reduced MC38 tumor growth over time (Fig. 5j) and tumor volume (Fig. 5k). Complete response (CR), where no tumor could be detected, and progressive disease (PD), where the treatment had no effect on tumor growth, were calculated for the MC38 tumor model at the end of the experiment. CR was observed for 1 of 12 (8%) tumors with ZT 4 treatment versus 4 of 14 (29%) tumors with ZT 16 treatment (Fig. 5j,k). PD was observed for 6 of 12 (50%) tumors with ZT 4 treatment versus 4 of 14 (29%) tumors with ZT 16 treatment (Fig. 5j,k). Notably, the CMT167 lung cancer line was less responsive to immunotherapy; however, a significant reduction in tumor volume was observed when

Fig. 5 | Time-of-day anti-PD-L1 treatment controls efficacy. a,**b**, Small intestinal Gr1$^+$ or Gr1$^+$PD-L1$^+$ cells as a percent of CD45$^+$ cells from WT and *Apc*$^{+/-}$;*Bmal1*$^{-/-}$ mice ($n = 8$ mice per group (**a**) and 5 mice per group (**b**)). **c**,**d**, Splenic Gr1$^+$ or Gr1$^+$PD-L1$^+$ cells as percent of CD45$^+$ cells from WT and *Apc*$^{+/-}$;*Bmal1*$^{-/-}$ mice ($n = 7$ mice per genotype (**c**), $n = 5$ mice per genotype (**d**)). For **a**–**d**, animals were killed at ZT 4 and ZT 16 and analyzed by flow cytometry. **e**, Graphical schematic of anti-PD-L1 administration experiment at two circadian time points. **f**, Spleen weight of *Apc*$^{+/-}$;*Bmal1*$^{-/-}$ mice untreated or treated with anti-PD-L1 at ZT 4 or ZT 16 ($n = 5$ mice per group). **g**,**h**, Small intestinal Gr1$^+$ cells or CD8$^+$ T cells as percent of CD45$^+$ cells from *Apc*$^{+/-}$;*Bmal1*$^{-/-}$ mice untreated or treated with anti-PD-L1 at ZT 4 or ZT 16 and analyzed by flow cytometry ($n = 6$ mice per group). **i**, Small intestinal polyp size from *Apc*$^{+/-}$;*Bmal1*$^{-/-}$ mice untreated or treated with anti-PD-L1 at ZT 4 or ZT 16 ($n = 70$ polyps per group). **j**, Tumor volume over time for WT mice after subcutaneous injection of MC38 cells and treatment with IgG or anti-PD-L1 at ZT 4 or ZT 16 ($n = 7$ mice per group). i.p., intraperitoneal. **k**, Tumor volume of WT mice 21 days after subcutaneous injection of MC38 cells and treatment with IgG or anti-PD-L1 at ZT 4 or ZT 16 ($n = 7$ mice per group, two tumors per mouse). **l**, Tumor volume of WT mice 18 days after subcutaneous injection of CMT167 cells and treatment with IgG or anti-PD-L1 at ZT 4 or ZT 16 ($n = 5$ mice per group, 2 tumors per mouse). **m**, Tumor volume of WT mice 12 days after subcutaneous injection of D4M-S cells and treatment with IgG or anti-PD-L1 at ZT 4 or ZT 16 ($n = 5$ mice per group, 2 tumors per mouse). Data represent the mean ± s.e.m. Statistical significance was determined by two-tailed Mann–Whitney *T*-test (**a**–**d**), one-way ANOVA with Tukey's multiple comparison (**f**–**i**,**k**–**m**) and two-way ANOVA with Tukey's multiple comparison (**j**). *$P < 0.05$; **$P < 0.01$; ***$P < 0.001$; ****$P < 0.0001$; NS, not significant.

https://doi.org/10.1038/s41590-024-01859-0

anti-PD-L1 was administered only at ZT 16 (Fig. 5l and Extended Data Fig. 10m). Finally, our data show that the D4M-S melanoma line is highly responsive to immunotherapy and ZT 16 administration of anti-PD-L1 was more effective at reducing tumor growth (Fig. 5m and Extended Data Fig. 10n). Taken together, these findings demonstrate that time-dependent regulation of PD-L1$^+$ MDSCs can be harnessed to promote the efficacy of immune checkpoint blockade in the treatment of CRC, as well as lung cancer and melanoma (Fig. 6).

Discussion

Circadian control of innate immunity plays a critical role in regulating the trafficking and recruitment of myeloid cells, such as monocytes,

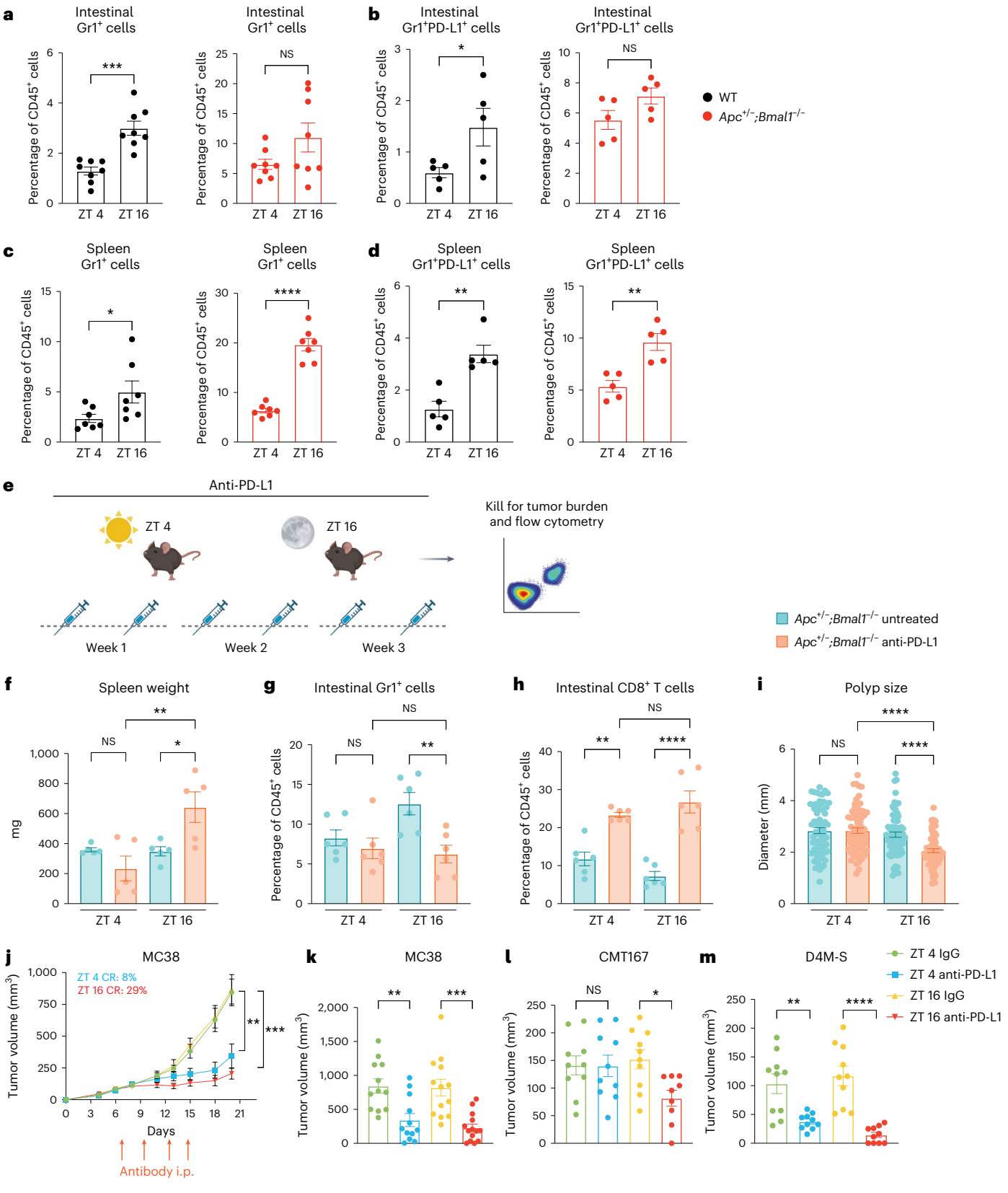

https://doi.org/10.1038/s41590-024-01859-0

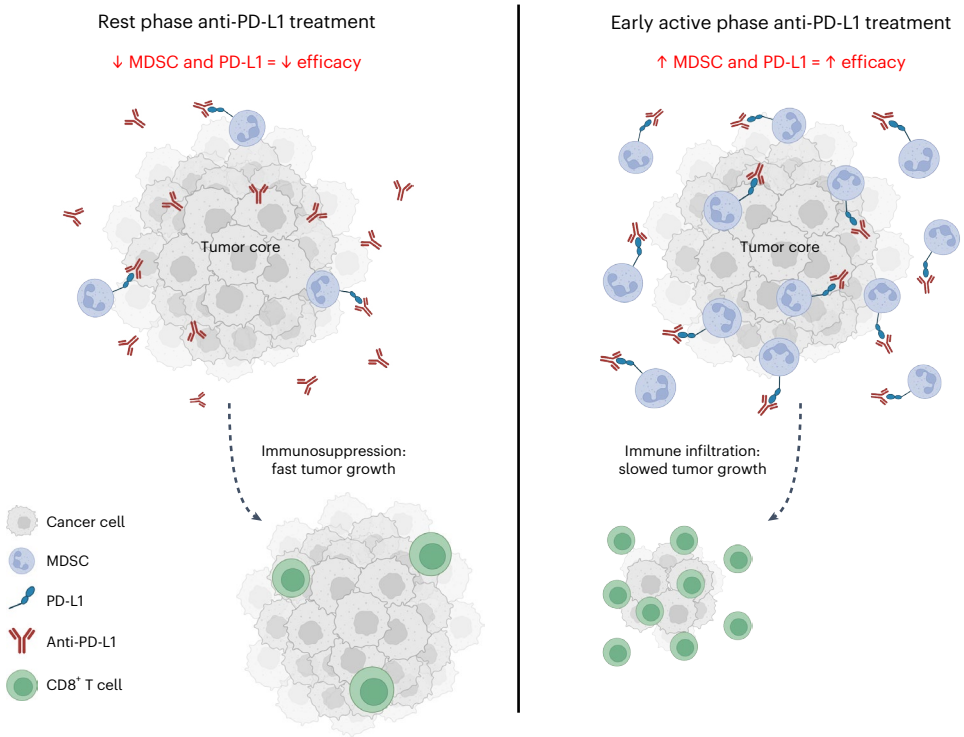

Fig. 6 | Model of circadian regulation of MDSCs for anti-PD-L1 treatment. MDSC abundance and PD-L1 expression are regulated by the circadian clock with a peak during the early active phase. By treating with anti-PD-L1 during the early active phase, when PD-L1 expressing MDSCs are most abundant, immune infiltration is stimulated and tumor growth is inhibited. The figure was created using biorender.com.

macrophages and neutrophils, which are essential components for host defense[13,16–18,76,77]. Additionally, tumor immunosurveillance has recently emerged as a dynamic process that also displays rhythmicity over the day–night cycle. Specifically, the rhythmic trafficking and function of DCs that governs tumor antigen presentation and subsequent priming of cytotoxic $CD8^+$ T cells controls tumor growth[20], and likely also governs rhythmic metastatic dissemination[19,78]. In addition to DC-dependent antigen processing by the circadian clock, it has been reported that efficacy of vaccination is time-of-day-dependent in both tumor and non-tumor models[20,77]. Therefore, we reasoned that the circadian clock likely dictates additional unknown factors that impinge on antitumor immunity, which could also inform therapeutic efficacy of immune checkpoint blockade.

Utilizing an unbiased scRNA-seq approach, we identified clock-dependent changes to the tumor immune landscape that govern immunosuppression. Mechanistically, our data support a model where an inherent crosstalk exists between epithelial and immune cells that is guided by the circadian clock network in the intestine. Disruption of the intestinal epithelial cell clock resulted in hyperactivation of pro-inflammatory cytokines and chemokines that promote neutrophil accumulation, MDSC development and immunosuppression. Given that the intestinal epithelium is highly Wnt-responsive, and clock disruption hyperactivates intestinal Wnt signaling (Fig. 4)[39], our data reveal a host of pro-inflammatory factors that are Wnt-dependent, clock-dependent or reliant on both pathways. Additionally, previous clinical studies have shown that in patients, MDSC accumulation is associated with advanced stage and metastatic CRC[72,73]. Our work now uncovers a previously unknown mechanism of MDSC control that is coordinately regulated by the circadian clock and Wnt signaling in the intestine.

Given the importance of the intestinal clock in regulating MDSCs, we now provide evidence that MDSC accumulation is time-of-day regulated (Fig. 5a–d). Our data illustrate that MDSCs peak in abundance at the beginning of the active phase, suggesting a temporal window of heightened immunosuppression. Previous studies have also shown that environmental clock disruption paradigms remodel the immune cell landscape including enhanced recruitment of macrophages and regulatory T cells[19,49]. Our findings now expand the repertoire of antitumor immunity to include clock-dependent control of immunosuppression through MDSCs. Based on these data, we leveraged this rhythmic control of immunosuppressive cells to show that timing of anti-PD-L1 delivery impacts treatment efficacy and outcome in models of CRC, lung cancer and melanoma (Fig. 5).

Finally, immunotherapy is not effective in all tumor types[79,80] and of ICI-responsive cancers, many patients subsequently demonstrate disease progression[7,8]. Circadian medicine approaches, including chronotherapy, suggest that timing of certain chemotherapies could provide therapeutic advantage when dosed at the optimal time of day[21–23]. We now provide evidence that immunotherapy follows a similar rationale based on the molecular underpinnings of clock-dependent control of immunosuppressive MDSCs within the tumor microenvironment. Moreover, retrospective analysis of clinical data suggest that dosing of ICIs during the early active phase could provide therapeutic benefit in multiple tumor types[27–30]. These clinical studies are in line with our findings and further support the need for prospective clinical trials investigating the time-of-day-dependent efficacy of immune checkpoint therapies in the treatment of solid tumors.

Online content

Any methods, additional references, Nature Portfolio reporting summaries, source data, extended data, supplementary information, acknowledgements, peer review information; details of author contributions and competing interests; and statements of data and code availability are available at https://doi.org/10.1038/s41590-024-01859-0.

References

1. Sinicrope, F. A. Increasing incidence of early-onset colorectal cancer. *N. Engl. J. Med.* **386**, 1547–1558 (2022).

2. Ben-Aharon, I. et al. Early-onset cancer in the gastrointestinal tract is on the rise—evidence and implications. *Cancer Discov.* **13**, 538–551 (2023).
3. Meulendijks, D. et al. Clinical relevance of DPYD variants c.1679T>G, c.1236G>A/HapB3, and c.1601G>A as predictors of severe fluoropyrimidine-associated toxicity: a systematic review and meta-analysis of individual patient data. *Lancet Oncol.* **16**, 1639–1650 (2015).
4. Sharma, P. & Allison, J. P. The future of immune checkpoint therapy. *Science* **348**, 56–61 (2015).
5. Diaz, L. A. et al. Pembrolizumab versus chemotherapy for microsatellite instability-high or mismatch repair-deficient metastatic colorectal cancer (KEYNOTE-177): final analysis of a randomised, open-label, phase 3 study. *Lancet Oncol.* **23**, 659–670 (2022).
6. André, T. et al. Pembrolizumab in microsatellite-instability-high advanced colorectal cancer. *N. Engl. J. Med.* **383**, 2207–2218 (2020).
7. Antonia, S. J. et al. Four-year survival with nivolumab in patients with previously treated advanced non-small-cell lung cancer: a pooled analysis. *Lancet Oncol.* **20**, 1395–1408 (2019).
8. Larkin, J. et al. Five-year survival with combined nivolumab and ipilimumab in advanced melanoma. *N. Engl. J. Med.* **381**, 1535–1546 (2019).
9. Takahashi, J. S. Transcriptional architecture of the mammalian circadian clock. *Nat. Rev. Genet.* **18**, 164–179 (2017).
10. Bass, J. & Lazar, M. A. Circadian time signatures of fitness and disease. *Science* **354**, 994–999 (2016).
11. Scheiermann, C., Gibbs, J., Ince, L. & Loudon, A. Clocking in to immunity. *Nat. Rev. Immunol.* **18**, 423–437 (2018).
12. Benitah, S. A. & Welz, P.-S. Circadian regulation of adult stem cell homeostasis and aging. *Cell Stem Cell* **26**, 817–831 (2020).
13. Gibbs, J. et al. An epithelial circadian clock controls pulmonary inflammation and glucocorticoid action. *Nat. Med.* **20**, 919–926 (2014).
14. Méndez-Ferrer, S., Lucas, D., Battista, M. & Frenette, P. S. Haematopoietic stem cell release is regulated by circadian oscillations. *Nature* **452**, 442–447 (2008).
15. Curtis, A. M., Bellet, M. M., Sassone-Corsi, P. & O'Neill, L. A. J. Circadian clock proteins and immunity. *Immunity* **40**, 178–186 (2014).
16. Gibbs, J. et al. The nuclear receptor REV-ERBα mediates circadian regulation of innate immunity through selective regulation of inflammatory cytokines. *Proc. Natl Acad. Sci. USA* **109**, 582–587 (2012).
17. Sutton, C. E. et al. Loss of the molecular clock in myeloid cells exacerbates T cell-mediated CNS autoimmune disease. *Nat. Commun.* **8**, 1923 (2017).
18. Nguyen, K. D. et al. Circadian gene Bmal1 regulates diurnal oscillations of Ly6C(hi) inflammatory monocytes. *Science* **341**, 1483–1488 (2013).
19. Hadadi, E. et al. Chronic circadian disruption modulates breast cancer stemness and immune microenvironment to drive metastasis in mice. *Nat. Commun.* **11**, 3193 (2020).
20. Wang, C. et al. Dendritic cells direct circadian anti-tumor immune responses. *Nature* **614**, 136–143 (2022).
21. Lévi, F. A. et al. Chronomodulated versus fixed-infusion-rate delivery of ambulatory chemotherapy with oxaliplatin, fluorouracil, and folinic acid (leucovorin) in patients with colorectal cancer metastases: a randomized multi-institutional trial. *J. Natl Cancer Inst.* **86**, 1608–1617 (1994).
22. Lévi, F., Zidani, R. & Misset, J. L. Randomised multicentre trial of chronotherapy with oxaliplatin, fluorouracil, and folinic acid in metastatic colorectal cancer. International Organization for Cancer Chronotherapy. *Lancet* **350**, 681–686 (1997).
23. Gou, X. X. et al. Induction chronomodulated chemotherapy plus radiotherapy for nasopharyngeal carcinoma: a phase II prospective randomized study. *J. Cancer Res. Ther.* **14**, 1613–1619 (2018).
24. Iacobelli, S. et al. A phase I study of recombinant interferon-α administered as a seven-day continuous venous infusion at circadian-rhythm modulated rate in patients with cancer. *Am. J. Clin. Oncol.* **18**, 27–31 (1995).
25. Deprés-Brummer, P. et al. A phase I trial of 21-day continuous venous infusion of α-interferon at circadian rhythm modulated rate in cancer patients. *J. Immunother.* **10**, 440–447 (1991).
26. Re, G. L. et al. Interleukin-2 chronotherapy for metastatic renal cell carcinoma: results of a phase I-II study. *Cytokine* **128**, 154984 (2020).
27. Qian, D. C. et al. Effect of immunotherapy time-of-day infusion on overall survival among patients with advanced melanoma in the USA (MEMOIR): a propensity score-matched analysis of a single-centre, longitudinal study. *Lancet Oncol.* **22**, 1777–1786 (2021).
28. Landre, T. et al. Time-dependent efficacy of immune checkpoint inhibitors in the treatment of metastatic cancers: a meta-analysis. *J. Clin. Oncol.* https://doi.org/10.1200/JCO.2023.41.16_suppl.2562 (2023).
29. Karaboué, A. et al. Time-dependent efficacy of checkpoint inhibitor nivolumab: results from a pilot study in patients with metastatic non-small-cell lung cancer. *Cancers* **14**, 896 (2022).
30. Yeung, C., Kartolo, A., Tong, J., Hopman, W. & Baetz, T. Association of circadian timing of initial infusions of immune checkpoint inhibitors with survival in advanced melanoma. *Immunotherapy* **15**, 819–826 (2023).
31. England, C. G. et al. Preclinical pharmacokinetics and biodistribution studies of 89Zr-labeled pembrolizumab. *J. Nucl. Med.* **58**, 162–168 (2017).
32. Papagiannakopoulos, T. et al. Circadian rhythm disruption promotes lung tumorigenesis. *Cell Metab.* **24**, 324–331 (2016).
33. Kettner, N. M. et al. Circadian homeostasis of liver metabolism suppresses hepatocarcinogenesis. *Cancer Cell* **30**, 909–924 (2016).
34. Lee, Donehower, L. A., Herron, A. J., Moore, D. D. & Fu, L. Disrupting circadian homeostasis of sympathetic signaling promotes tumor development in mice. *PLoS ONE* **5**, e10995 (2010).
35. Stokes, K. et al. The circadian clock gene, Bmal1, regulates intestinal stem cell signaling and represses tumor initiation. *Cell. Mol. Gastroenterol. Hepatol.* **12**, 1847–1872 (2021).
36. Pariollaud, M. et al. Circadian disruption enhances HSF1 signaling and tumorigenesis in Kras-driven lung cancer. *Sci. Adv.* https://doi.org/10.1126/sciadv.abo1123 (2022).
37. Fu, L., Pelicano, H., Liu, J., Huang, P. & Lee, C. C. The circadian gene Period2 plays an important role in tumor suppression and DNA damage response in vivo. *Cell* **111**, 41–50 (2002).
38. Wood, P. A. et al. Period 2 mutation accelerates ApcMin/+ tumorigenesis. *Mol. Cancer Res.* **6**, 1786–1793 (2008).
39. Chun, S. K. et al. Disruption of the circadian clock drives Apc loss of heterozygosity to accelerate colorectal cancer. *Sci. Adv.* **8**, 2389 (2022).
40. Fekry, B. et al. Incompatibility of the circadian protein BMAL1 and HNF4α in hepatocellular carcinoma. *Nat. Commun.* **9**, 4349 (2018).
41. Sulli, G. et al. Pharmacological activation of REV-ERBs is lethal in cancer and oncogene-induced senescence. *Nature* **553**, 351–355 (2018b).
42. Dong, Z. et al. Targeting glioblastoma stem cells through disruption of the circadian clock. *Cancer Discov.* **9**, 1556–1573 (2019).

43. Chen, P. et al. Circadian regulator CLOCK recruits immune-suppressive microglia into the GBM tumor microenvironment. *Cancer Discov.* **10**, 371–381 (2020).
44. Cheung, A. F. et al. Complete deletion of Apc results in severe polyposis in mice. *Oncogene* **29**, 1857–1864 (2010).
45. Wei, Y. et al. B cell heterogeneity, plasticity, and functional diversity in cancer microenvironments. *Oncogene* **40**, 4737–4745 (2021).
46. Liu, R.-X. et al. Altered B cell immunoglobulin signature exhibits potential diagnostic values in human colorectal cancer. *iScience* **26**, 106140 (2023).
47. Shalapour, S. & Karin, M. The neglected brothers come of age: B cells and cancer. *Semin. Immunol.* **52**, 101479 (2021).
48. Oosterman, J. E., Wopereis, S. & Kalsbeek, A. The circadian clock, shift work, and tissue-specific insulin resistance. *Endocrinology* **161**, bqaa180 (2020).
49. Aiello, I. et al. Circadian disruption promotes tumor-immune microenvironment remodeling favoring tumor cell proliferation. *Sci. Adv.* **6**, eaaz4530 (2020).
50. Alshetaiwi, H. et al. Defining the emergence of myeloid-derived suppressor cells in breast cancer using single-cell transcriptomics. *Sci. Immunol.* **5**, eaay6017 (2020).
51. Huang, B. et al. Gr-1^{+}CD115^{+} immature myeloid suppressor cells mediate the development of tumor-induced T regulatory cells and T-cell anergy in tumor-bearing host. *Cancer Res.* **66**, 1123–1131 (2006).
52. Zhao, H. et al. Myeloid-derived itaconate suppresses cytotoxic CD8^{+} T cells and promotes tumour growth. *Nat. Metab.* **4**, 1660–1673 (2022).
53. Jou, E. et al. An innate IL-25–ILC2–MDSC axis creates a cancer-permissive microenvironment for *Apc* mutation–driven intestinal tumorigenesis. *Sci. Immunol.* **7**, eabn0175 (2022).
54. Youn, J.-I., Nagaraj, S., Collazo, M. & Gabrilovich, D. I. Subsets of myeloid-derived suppressor cells in tumor bearing mice. *J. Immunol.* **181**, 5791–5802 (2008).
55. Kusmartsev, S. A., Li, Y. & Chen, S.-H. Gr-1^{+} myeloid cells derived from tumor-bearing mice inhibit primary T cell activation induced through CD3/CD28 costimulation1. *J. Immunol.* **165**, 779–785 (2000).
56. Klement, J. D. et al. Tumor PD-L1 engages myeloid PD-1 to suppress type I interferon to impair cytotoxic T lymphocyte recruitment. *Cancer Cell* **41**, 620–636.e9 (2023).
57. Noman, M. Z. et al. PD-L1 is a novel direct target of HIF-1α, and its blockade under hypoxia enhanced MDSC-mediated T cell activation. *J. Exp. Med.* **211**, 781–790 (2014).
58. Nusse, R. & Clevers, H. Wnt/β-catenin signaling, disease, and emerging therapeutic modalities. *Cell* **169**, 985–999 (2017).
59. Casey, S. C. et al. MYC regulates the anti-tumor immune response through CD47 and PD-L1. *Science* **352**, 227–231 (2016).
60. Kortlever, R. M. et al. Myc cooperates with Ras by programming inflammation and immune suppression. *Cell* **171**, 1301–1315 (2017).
61. Kozuka, K. et al. Development and characterization of a human and mouse intestinal epithelial cell monolayer platform. *Stem Cell Rep.* **9**, 1976–1990 (2017).
62. Coffelt, S. B. et al. IL-17-producing γδ T cells and neutrophils conspire to promote breast cancer metastasis. *Nature* **522**, 345–348 (2015).
63. Zhao, H. et al. Inflammation and tumor progression: signaling pathways and targeted intervention. *Signal Transduct. Target. Ther.* **6**, 1–46 (2021).
64. Ban, Y. et al. Targeting autocrine CCL5–CCR5 axis reprograms immunosuppressive myeloid cells and reinvigorates antitumor immunity. *Cancer Res.* **77**, 2857–2868 (2017).
65. Ernst, M. & Putoczki, T. IL-17 cuts to the chase in colon cancer. *Immunity* **41**, 880–882 (2014).
66. Chung, A. S. et al. An interleukin-17–mediated paracrine network promotes tumor resistance to anti-angiogenic therapy. *Nat. Med.* **19**, 1114–1123 (2013).
67. Borish, L. C. & Steinke, J. W. Cytokines and chemokines. *J. Allergy Clin. Immunol.* **111**, S460–S475 (2003). 2.
68. Kohli, K., Pillarisetty, V. G. & Kim, T. S. Key chemokines direct migration of immune cells in solid tumors. *Cancer Gene Ther.* **29**, 10–21 (2022).
69. Santos, I. et al. CXCL5-mediated recruitment of neutrophils into the peritoneal cavity of Gdf15-deficient mice protects against abdominal sepsis. *Proc. Natl Acad. Sci. USA* **117**, 12281–12287 (2020).
70. Besnard, A.-G. et al. CXCL6 antibody neutralization prevents lung inflammation and fibrosis in mice in the bleomycin model. *J. Leukoc. Biol.* **94**, 1317–1323 (2013).
71. Pelka, K. et al. Spatially organized multicellular immune hubs in human colorectal cancer. *Cell* **184**, 4734–4752.e20 (2021).
72. Zhang, B. et al. Circulating and tumor-infiltrating myeloid-derived suppressor cells in patients with colorectal carcinoma. *PLoS ONE* **8**, e57114 (2013).
73. Karakasheva, T. A. et al. CD38^{+} M-MDSC expansion characterizes a subset of advanced colorectal cancer patients. *JCI Insight* **3**, e97022 (2018).
74. Huang, T. et al. Wnt inhibition sensitizes PD-L1 blockade therapy by overcoming bone marrow-derived myofibroblasts-mediated immune resistance in tumors. *Front. Immunol.* **12**, 619209 (2021).
75. Pilato, M. D. et al. Targeting the CBM complex causes Treg cells to prime tumors for immune checkpoint therapy. *Nature* **570**, 112–116 (2019).
76. Roberts, N. T., MacDonald, C. R., Mohammadpour, H., Antoch, M. P. & Repasky, E. A. Circadian rhythm disruption increases tumor growth rate and accumulation of myeloid-derived suppressor cells. *Adv. Biol.* **6**, 2200031 (2022).
77. Cervantes-Silva, M. P. et al. The circadian clock influences T cell responses to vaccination by regulating dendritic cell antigen processing. *Nat. Commun.* **13**, 7217 (2022).
78. Diamantopoulou, Z. et al. The metastatic spread of breast cancer accelerates during sleep. *Nature* **607**, 156–162 (2022).
79. Ferris, R. L. et al. Durvalumab with or without tremelimumab in patients with recurrent or metastatic head and neck squamous cell carcinoma: EAGLE, a randomized, open-label phase III study. *Ann. Oncol.* **31**, 942–950 (2020).
80. Garg, A. D. et al. Preclinical efficacy of immune-checkpoint monotherapy does not recapitulate corresponding biomarkers-based clinical predictions in glioblastoma. *Oncoimmunology* **6**, e1295903 (2017).

Methods

Mice

Apc mice that harbor a heterozygous floxed allele of exons 1 to 15 ($Apc^{+/\Delta ex1-15}$)[44] were crossed with *Bmal1* conditional mice that carry homozygous floxed alleles of exon 8 ($Bmal1^{fl/fl}$)[81]. Intestine-specific targeting of epithelial cells was achieved by crossing these conditional mice with Villin-Cre animals to create $Apc^{+/\Delta ex1-15}$;$Bmal1^{fl/fl}$;*Villin-Cre* mice. All mouse strains are on a C57BL/6 background and both males and females aged 9–10 months were used for experiments. Mice were purchased from the Jackson Laboratory. All experiments were performed in accordance with the Institutional Animal Care and Use Committee guidelines at the University of California, Irvine. Animals were housed on a standard 12-h light–dark paradigm, with temperatures of 65–75 °F, humidity 40–60% and fed ad libitum. The environmental SD paradigm was performed on 2-month-old WT mice purchased from the Jackson Laboratory. Mice were shifted for 1–8 weeks by advancing the light phase by 8 h every other day. For the circadian ZT 4 and ZT 16 experiments, WT and $Apc^{+/-}$;$Bmal1^{-/-}$ mice were divided into two groups. One group was kept in normal 12-h LD conditions and the other group was kept in an inverted 12-h DL condition to perform flow cytometry at the same time.

Spleen tissue collection and cell isolation

Animals were killed at the ZT indicated in the legend, spleens were quickly excised, pushed through a 70-µm cell strainer to create a cell suspension of splenocytes and washed with RPMI. Cells were centrifuged at 500*g* at 4 °C for 10 min and then incubated for 1 min in 5 ml RBC lysis buffer at RT. Cells were quenched with 10 ml serum-free PBS and pelleted by centrifugation at 500*g* at 4 °C for 5 min. Cells were resuspended in 5 ml FACS buffer (1× PBS with 10% FBS) and total remaining live cells were counted by Countess II and processed for downstream FACS analysis.

Small intestine tissue collection and cell isolation

Tissue samples were collected from mice at the ZT indicated in the legend, flushed and cut longitudinally. Tissues were placed in RPMI medium containing 1% FBS, 18 µg ml^{-1} DNase1 (Sigma-Aldrich, 04536282001) and 0.6 mg ml^{-1} Collagenase type P (Roche, 11249002001) and were digested at 37 °C on a shaker for 30 min. Cells were filtered through a 70-µm cell strainer, washed with PBS containing 1 M HEPES and 2% FBS. Samples were centrifuged to pellet cells, which were then resuspended in RPMI medium, filtered through a 40-µm cell strainer and washed with PBS containing 1 M HEPES and 2% FBS. Cells were centrifuged at 500*g* at 4 °C for 5 min and then incubated for 1 min in 1 ml RBC lysis buffer at RT. Cells were quenched with 10 ml serum-free PBS and centrifuged at 500*g* at 4 °C for 5 min. Cells were resuspended in 1 ml FACS buffer (1× PBS with 10% FBS) and total remaining live cells were counted by Countess II and processed for FACS analysis.

Lymph node collection and cell isolation

The mesenteric draining lymph node was collected at the ZT indicated in the legend and teased open with a 23G needle before being placed in digestion solution containing 1 mg ml^{-1} Collagenase D and A. After incubating at 37 °C on a shaker for 20 min, cells were filtered through a 70-µm cell strainer and washed with PBS. Samples were centrifuged to pellet cells, which were then resuspended in 1 ml FACS buffer (1× PBS with 10% FBS) and total remaining live cells were counted by Countess II and processed for FACS analysis.

Bone marrow collection and cell isolation

The femur and tibia were collected and flushed with HBSS supplemented with 2% FBS and 1 mM EDTA using a 25G needle. Cells were centrifuged at 500*g* at 4 °C for 5 min, washed with 5 ml HBSS supplemented with 2% FBS and 1 mM EDTA and filtered through a 70-µm cell strainer. The total remaining live cells were counted by Countess II.

Blood collection and cell isolation

Blood was collected at the ZT indicated in the legend by cardiac puncture and 0.5 M EDTA was added to blood at a ratio of 1:10. Blood was incubated for 5 min in 2 ml RBC lysis buffer at RT. Cells were quenched with 10 ml serum-free PBS and centrifuged at 500*g* at 4 °C for 5 min. Red blood cell lysis was repeated again and then cells were resuspended in 1 ml FACS buffer (1× PBS with 10% FBS) and total remaining live cells were counted by Countess II and processed for FACS analysis.

Fluorescence-activated cell sorting

Tissue samples were collected from mice at the ZT indicated in the legend and mechanically dissociated to generate single cell suspensions as described above. Cells were blocked with anti-mouse FcγR (CD16/CD32) (BioLegend, 101301) on ice for 5 min. Cells were then centrifuged at 400*g* for 3 min at 4 °C and washed once with FACS buffer (1× PBS with 10% FBS). Cells were incubated for 30 min at 4 °C with pre-conjugated fluorescent labeled antibodies with the following combinations: CD45 (BioLegend, 103112 (APC)), CD11b (BioLegend, 101228 (PerCP/cyanine5.5), 101205 (FITC) or 101225 (APC/Cy7)), Gr1 (BioLegend, 108439 (BV605) or 108407 (PE)), F4/80 (BioLegend, 123110 (PE)), Ly6C (BioLegend, 128035 (BV605)), Ly6G (BioLegend, 127606 (FITC)), CD3 (TONBO Biosciences, 50-0032 (PE)), CD4 (Life Technologies, 46-0042-82 (eFluor710)), CD8 (RndSystems, FAB116G (AlexaFluor488)), CD25 (BioLegend, 102037 (BV650)) and PD-L1 (Tonbo Biosciences, 50-1243 (PE)). Sytox Blue dye (Life Technologies, S34857) was added to stained cells to assay for viability. Cells were sorted by BD FACSAria Fusion and desired populations were isolated for downstream experiments. Data were analyzed using FlowJo software v.10.0.7 (Tree Star).

T cell suppression assay

Spleens were dissected, filtered into a single-cell suspension and depleted of red blood cells using Tris-acetic-acid-chloride. T cells were isolated from the spleen using the EasySep Mouse T cell Isolation kit (STEMCELL Technologies, 19851) according to the manufacturer's instructions. Isolated T cells were washed once with PBS and resuspended at 15×10^6 ml^{-1} in staining buffer (0.01% BSA in PBS). T cells were stained with proliferation dye eFluor 670 (Thermo Fisher Scientific, 65-0840-85) using 5 mM dye per 1×10^7 cells and incubated in a 37 °C water bath for 10 min. Finally, T cells were washed and resuspended at 1×10^6 ml^{-1} in RPMI 1640 with HEPES + L-glutamine complete medium containing 10% FBS, 1× non-essential amino acids, 100 U ml^{-1} penicillin, 100 µg ml^{-1} streptomycin, 1 mM sodium pyruvate and 55 µM β-mercaptoethanol. eFluor 670-labeled T cells were plated (50×10^3 per well) in a U-bottom 96-well plate and activated with plate bound anti-Armenian hamster IgG (30 µg ml^{-1}, Jackson ImmunoResearch, 127-005-099), with CD3 (0.5 µg ml^{-1}, Tonbo, 70–0031) and CD28 (1 µg ml^{-1}, Tonbo, 70–0281). Sorted CD11b$^+$ Gr1$^+$ cells were added to T cells in 1:1 ratio (50×10^3 T cells: 50×10^3 CD11b$^+$ Gr1$^+$ cells). After 3 days of culture, cells were collected and blocked with anti-mouse CD16/32 (BioLegend, 101302), stained with Zombie Live/Dead Dye (BioLegend, 423105) and fluorescent-conjugated antibodies: CD4 (BioLegend, 100512; clone RM4–5) and CD8 (BioLegend, 100709; clone 53–6.7). Single-stained samples and fluorescence minus one controls were used to establish PMT voltages, gating and compensation parameters. Cells were processed using the BD FACSAria Fusion flow cytometer and analyzed using FlowJo software v.10.0.7 (Tree Star).

ROS production assay

Cells were collected from respective tissues and processed to single cell suspensions as described above. Cells were stained with CD45, CD11b and Gr1 antibodies as described above. Following staining, cells were resuspended in FACS buffer and 10 mM H_2DCFDA (Sigma-Aldrich, D6883) was added and incubated for 30 min at room temperature. Cells were then processed on the BD FACSAria Fusion and analyzed using FlowJo software v.10.0.7 (Tree Star).

Cytokine/chemokine ELISA

WT and *Bmal1*$^{-/-}$ primary intestinal monolayers were cultured with or without 100 ng ml^{-1} recombinant mouse Wnt3a (Peprotech, 315-20). Undiluted CM and cell lysate were profiled using the 32-plex Discovery Assay (Mouse Cytokine/Chemokine 32-Plex Panel, Eve Technologies).

Primary neutrophil assays

Neutrophils were isolated from mouse bone marrow using the EasySep Mouse Neutrophil Enrichment kit (STEMCELL Technologies, 19762). For the migration assay, 1 million neutrophils were plated in the top well of a 24-well Transwell insert (Corning, 3378) and WT or *Bmal1*$^{-/-}$ intestinal monolayer CM was added to the bottom well. After 18 h, neutrophils that migrated to the bottom well were counted. For the culture with intestinal monolayer CM, 500,000 neutrophils were plated in a 24-well plate with intestinal monolayer CM. After 24 h, neutrophils were collected for RNA isolation and qPCR analysis.

Mouse intestinal organoid isolation and culturing

The following protocol for isolation and culture of mouse intestinal organoids was used with minor modifications, based on previously published methods[82]. The intestinal segment was dissected into small pieces and incubated in dissociation solution (PBS supplemented with 2 mM EDTA and 10 µM Rho kinase inhibitor Y-27632) for 1 h at 4 °C with agitation. Next, intestinal tissue pieces were shaken, strained and centrifuged. Pellets were resuspended in Matrigel (Corning) and ENR medium was added. ENR is a basal medium supplemented with recombinant murine EGF (50 ng ml^{-1}) (PeproTech), recombinant murine Noggin (50 ng ml^{-1}) (PeproTech), 1 mM *N*-acetylcysteine (Sigma-Aldrich) and 20% (v/v) of R-Spondin CM (*Rspo1*-expressing cells, Trevigen). The basal medium was advanced Dulbecco's modified Eagle's medium (DMEM)/F12 (Gibco) supplemented with 3 mM L-glutamine (Thermo Fisher Scientific), Primocin (100 µg ml^{-1}) (InvivoGen), and 10 mM HEPES (Sigma-Aldrich). For primary intestinal epithelial monolayer culture, dissociated intestinal tissues were centrifuged and resuspended in ENR medium supplemented with Y-27632 (Biogems) and 10 µM CHIR-99021 (Sigma-Aldrich), and then seeded on top of a Matrigel-coated cell culture plate.

Immunoblots

Organoid pellets were lysed in radioimmunoprecipitation assay lysis buffer (50 mM tris (pH 8), 150 mM NaCl, 5 mM EDTA, 15 mM $MgCl_2$ and 1% NP-40) containing protease and phosphatase inhibitors (1× complete EDTA free cocktail tablet (Sigma-Aldrich), 0.5 mM phenylmethylsulfonyl fluoride, 20 mM NaF, 1 mM Na_3VO_4, 1 µM trichostatin A and 10 mM nicotinamide). Protein lysates were resolved on an SDS polyacrylamide gel. Antibodies used for immunoblots were c-MYC (Abcam, ab32072) and p84 (GeneTex, GTX70220).

Lentiviral transduction of organoids

The third-generation lentiviral packaging system was used for transduction of intestinal organoids. For production of viral particles, HEK293T cells were transfected with plasmids encoding lentiviral packaging (pRSV-Rev and pMDLg/pRRE), lentiviral envelope (pMD2.G) and the desired transfer vector. Lentivirus-containing medium was collected 48 h after transfection, filtered through a 0.45-µm syringe filter and concentrated over 100-fold in volume by ultracentrifugation. For transduction of organoid monolayers, virus was incubated with 10 µg ml^{-1} polybrene in medium supplemented with Y-27632 (Biogems) and 10 µM CHIR-99021 (Sigma-Aldrich). Primary intestinal monolayers were collected 48 h later. For the lentiviral transduction of *c-Myc* shRNA in WT intestinal monolayers, Lenti-sh1368 plasmid was used (Addgene, 29435).

Single-cell RNA sequencing

FACS-sorted CD45$^+$ cells were isolated at ZT 4 from the small intestine of 9–10-month-old WT, *Bmal1*$^{-/-}$, *Apc*$^{+/-}$ and *Apc*$^{+/-}$;*Bmal1*$^{-/-}$ mice ($n = 3$ mice per genotype). Cells were washed once in PBS with 0.04% BSA, and a total of 0.2–2 × 10^6 cells per genotype were used for cell multiplexing barcoding using the CellPlex kit (10x Genomics), according to manufacturer's instructions. In brief, cells were pelleted after washing by centrifugating at 300 rcf for 5 min at room temperature and resuspended in 100 µl Cell Multiplexing oligonucleotides (one oligonucleotide/barcode per genotype). Oligonucleotides were allowed to bind cell membranes by incubating at room temperature for 5 min and unbound multiplexing oligonucleotides were washed three times with 2 ml ice-cold PBS + 1% BSA. After washing, cells were resuspended in chilled PBS + 1% BSA to a concentration of approximately 1,000 cells per µl, and loaded onto the 10x Genomics Chromium Controller for droplet-enabled scRNA-seq according to the manufacturer's instructions. Library generation was performed following the Chromium NextGEM Single Cell v.3.1 Cell Multiplexing Reagents Kits User Guide: CG000388Rev B. A total of three libraries were generated, each of them consisting of a pool of equal cell numbers from CD45$^+$ cells from the small intestine of each genotype. Multiplexed, single cell gene expression libraries were sequenced on the Illumina HiSeq. Alignment of 3′ end counting libraries from scRNA-seq analyses was completed utilizing 10x Genomics CellRanger v.6.1.2. Each library was aligned to an indexed mm10 genome using cellranger count.

Mouse scRNA-seq data analysis

All scRNA-seq analysis was performed in R (v.4.2.1) using Rstudio (v.2023.03.1 Build 446) and the Seurat v.4 package[83]. CellRanger outputs were loaded into R using the Read10X() function and Seurat objects from each sample were generated using the CreateSeuratObject() function, where genes that were not detected in at least three cells (min.cells = 3) and cells containing fewer than 200 different genes (min.features = 200) were excluded. Seurat objects containing single cell gene expression data from each sample were merged using the merge() function and percentages of mitochondrial genes (percent.mt) expressed in each cell were calculated using the PercentageFeatureSet() function. Low-quality cells were filtered out from Seurat objects utilizing the subset() function, where only cells with nFeature_RNA > 200 and <8,000 and percent.mt < 20 were carried forward in the analysis. After removing low-quality cells, Seurat objects were normalized using the NormalizeData() function, using the 'LogNormalize' method and a scale factor of 10,000. After normalization, the top 2,000 most variable genes were calculated using the FindVariableFeatures() function, utilizing the vst selection method. Data were then scaled for dimensionality reduction using the ScaleData() function and linear dimensionality reduction was calculated with the RunPCA() function using the variable features. Then, the FindNeighbors() function and the RunUMAP() functions were run using 20 PCs. Clustering was achieved using the FindClusters() function and cluster identities were manually assigned after examining the top expressed genes in each cluster using the FindAllMarkers() function. The function FindAllMarkers() performs differential gene expression between two groups using the Wilcoxon rank-sum test by default, which are then plotted in the heat maps produced with DoHeatmap() where the selected number of top genes per cell cluster are shown. This function only returns genes that have a *P* value below the specified threshold (default = 0.01). This provided data for 17,692 cells. The data were analyzed again for low-quality cells; this time, cells with nFeature < 3,000 and percent.mt < 10 were additionally excluded. This step reduced the data to 15,234 cells. For T cell and myeloid subclustering, the data were subset by appropriate cell types: 'neutrophils' and 'monocytes/macrophages/dendritic cells' for the myeloid subclustering and 'CD4 T cells', 'CD8 T cells' and 'double-negative (DN) T cells' for the T cell subclustering. Then, normalization, scaling and immune cell marker analysis were performed again. To additionally analyze cell types highly expressing PD-L1 (CD274), subsetting was performed with cells having PD-L1 expression > 2.

RNA extraction and gene expression analysis

Total RNA from sorted single cells was extracted using a Direct-zol RNA microprep kit (Zymo Research). To generate cDNA, equal amounts of total RNA were incubated with Maxima H Minus cDNA Synthesis Master Mix (Thermo Fisher Scientific) according to the manufacturer's instructions. cDNA was used for quantitative real-time PCR using PowerUp SYBR Green Master Mix (Applied Biosystems). Gene expression was normalized to 18S ribosomal RNA. Primer sequences used for gene expression analysis by qPCR are listed in Table 1.

Human scRNA-seq data analysis

All human scRNA-seq analysis was performed in R (v.4.2.1) using Rstudio (v.2023.03.1 Build 446) and the Seurat v.4 package[83]. Data were obtained from Pelka et al.[71], downloaded and converted into a Seurat object. Percentages of mitochondrial genes (percent.mt) expressed in each cell were calculated using the PercentageFeatureSet() function. The data had been prefiltered by Pelka et al. to percent.mt < 50, and this was determined as the optimal threshold. Low-quality cells were filtered out from Seurat objects utilizing the subset() function, where only cells with nFeature_RNA > 200 and <8,000 and nCount_RNA < 10,000 were carried forward in the analysis. After removing low-quality cells, the Seurat object was additionally subset to cells expressing CD45 (PTPRC) > 0.5 to focus on immune cells, resulting in 82,611 cells. The object was then normalized using the NormalizeData() function, using the 'LogNormalize' method and a scale factor of 10,000. After normalization, the top 5,000 most variable genes were calculated using the FindVariableFeatures() function, utilizing the vst selection method. Data were then scaled for dimensionality reduction using the ScaleData() function, and linear dimensionality reduction was calculated with the RunPCA() function using the variable features. Then, the FindNeighbors() and the RunUMAP() functions were run using 20 PCs. Clustering was achieved using the FindClusters() function with a resolution of 0.8, and cluster identities were manually assigned after examining the expression of immune-lineage specific genes in each cluster using the DotPlot() function (Extended Data Fig. 9a). The function FindAllMarkers() performs differential gene expression between two groups using the Wilcoxon rank-sum test by default, which are then plotted in the heat maps produced with DoHeatmap() where the selected number of top genes per cell cluster are shown. This function only returns genes that have a *P* value below the specified threshold (default = 0.01). To appropriately compare normal and tumor tissue, final analyses were reported after subsetting to only immune cell data from patients with matched tumor and normal tissue samples, resulting in 55,535 cells from 36 patients. Expression of PD-L1 (CD274) was additionally analyzed by subsetting the object to cells with PD-L1 expression >0, resulting in 1,253 cells.

Anti-PD-L1 treatment in *Apc*$^{+/-}$;*Bmal1*$^{-/-}$ mice

Apc$^{+/-}$;*Bmal1*$^{-/-}$ mice were randomized into two groups, ZT 4 and ZT 16. For injections to be performed at the same time of day, ZT 16 mice were put in a separate room with an inverted light schedule. Mice were subjected to a gradual shift in time (1 h d^{-1}) to minimize systemic circadian disruption. Anti-PD-L1 (BioLegend, 124329) was administered twice weekly (200 µg per mouse) by intraperitoneal injection. After 3 weeks, mice were killed for tumor burden and flow cytometric analysis.

Anti-PD-L1 treatment in subcutaneous tumor models

Mice received a subcutaneous injection of 1×10^6 MC38 cells, 2×10^6 D4M-S cells or 2×10^6 CMT167 cells per tumor at ZT 4. Cells were resuspended in Matrigel to facilitate engraftment. Two tumors were injected per mouse 1 cm off the midline in both sides of the abdomen. IgG (BioLegend, 400668) or anti-PD-L1 (BioLegend, 124329) were administered every 2–3 days (200 µg per mouse) for a total of four treatments by intraperitoneal injection. Mice were killed before the tumor size exceeded 1,000 mm^3.

Statistical analysis

Sample sizes were calculated using the proper power analysis test for either *t*-test or one-way ANOVA and a confidence of 90%. Data distribution was assumed to be normal but this was not formally tested. Statistical analyses were performed in Prism v.10 (GraphPad Software). Visualization was performed using Prism v.10 (GraphPad Software), Seurat or ggplot2(). All resulting graphs are shown as mean ± s.e.m. with details of the statistical test used specified in the legend. Animals were randomized before beginning experiments and data collection and analyses were not performed blind.

Reporting summary

Further information on research design is available in the Nature Portfolio Reporting Summary linked to this article.

Data availability

scRNA-seq data have been deposited at the NCBI Gene Expression Omnibus under accession code GSE262267 and in the Sequence Read Archive under accession code PRJNA1003452. Source data are provided with this paper.

References

81. Storch, K.-F. et al. Intrinsic circadian clock of the mammalian retina: importance for retinal processing of visual information. *Cell* **130**, 730–741 (2007).
82. Sato, T. et al. Single Lgr5 stem cells build crypt-villus structures in vitro without a mesenchymal niche. *Nature* **459**, 262–265 (2009).
83. Hao, Y. et al. Integrated analysis of multimodal single-cell data. *Cell* **184**, 3573–3587 (2021).

Acknowledgements

B.M.F. and S.M.P. were supported by the National Cancer Institute (NCI) T32 Interdisciplinary Cancer Research Training Program (grant no. T32CA009054) and B.M.F. was also supported by the NCI grant F31CA287992. A.L.M. was supported by the National Science Foundation Graduate Research Fellowship Program (grant no. DGE1839285). A.M. was supported by the NCI grant F31AR083279. We acknowledge the support of the Chao Family Comprehensive Cancer Center at the University of California, Irvine, which is supported by the NCI (P30 CA062203). Shared resources included use of the Genomics Research and Technology Hub. We thank the Institute for Immunology Flow Cytometry Facility and the Stem Cell Flow Core at the University of California, Irvine for technical assistance. The Pannunzio laboratory is supported by National Institutes of Health (NIH)/NCI grants R37CA266042 and R01CA276470. The Seldin laboratory is supported by the NIH/National Institute of Diabetes and Digestive and Kidney Diseases grant DP1DK130640. The Marangoni laboratory is supported by the Melanoma Research Alliance Bristol Meyers Squibb Young Investigator Award no. 929155 and the DoD Team grant ME220176P1. Financial support for the Masri laboratory is provided through the NIH/NCI (R01CA244519 and R01CA259370), the V Foundation for Cancer Research and Johnson & Johnson.

Author contributions

Conceptualization was the responsibility of B.M.F. and S.M. Methodology was the responsibility of B.M.F., J.I.R., H.A., O.S.E., N.R.P., M.M.S., I.M., F.M., D.A.L., and K.K. Investigation was carried out by B.M.F., S.M.P., J.I.R., H.A., A.N.L., A.M., W.A.S., A.L.M., S.K.C., A.H., I.A. and M.M.S. Visualization was carried out by B.M.F. and S.M.P. Supervision was carried out by S.M. B.M.F., S.M.P. and S.M. were responsible for writing.

Competing interests
The authors declare no competing interests.

Additional information
Extended data is available for this paper at https://doi.org/10.1038/s41590-024-01859-0.

Supplementary information The online version contains supplementary material available at https://doi.org/10.1038/s41590-024-01859-0.

Correspondence and requests for materials should be addressed to Selma Masri.

Peer review information *Nature Immunology* thanks Dmitry Gabrilovich and the other, anonymous, reviewer(s) for their contribution to the peer review of this work. Primary Handling Editor: N. Bernard, in collaboration with the *Nature Immunology* team.

https://doi.org/10.1038/s41590-024-01859-0

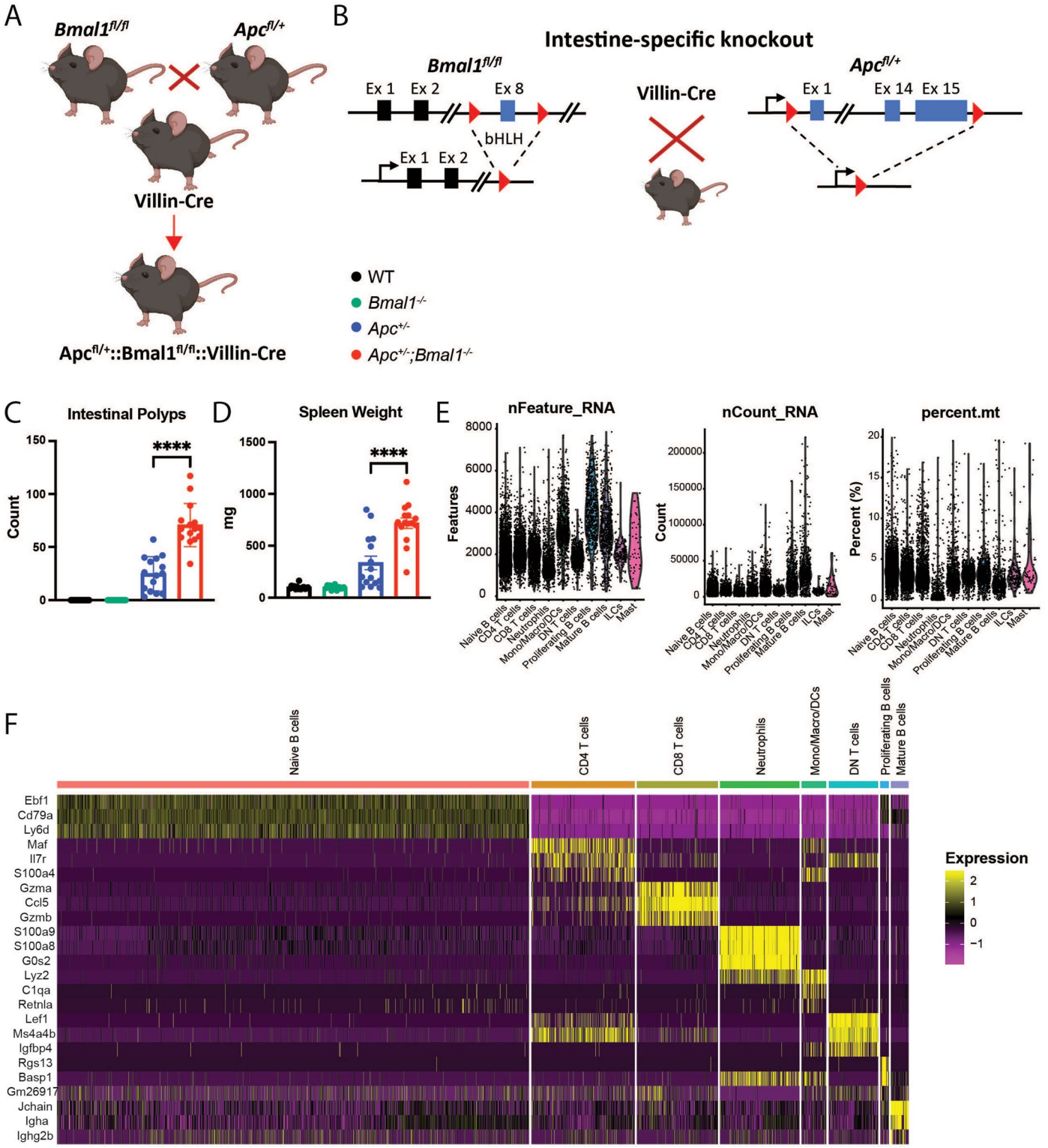

Extended Data Fig. 1 | Circadian clock disruption promotes intestinal tumorigenesis. (a) Graphic of mouse genotypes. **(b)** Gene targeting strategy for generation of intestine-specific knockout of *Bmal1* and *Apc*. (**c**) Small intestinal polyp count from WT, *Bmal1*$^{-/-}$, *Apc*$^{+/-}$, and *Apc*$^{+/-}$;*Bmal1*$^{-/-}$ mice (n = 15 mice/genotype). (**d**) Spleen weight from WT, *Bmal1*$^{-/-}$, *Apc*$^{+/-}$, and *Apc*$^{+/-}$;*Bmal1*$^{-/-}$ mice (n = 15 mice/genotype). (**e**) Violin plots of RNA features, count, and percent of mitochondrial RNA for each immune cell cluster prior to filtering mitochondrial RNA < 10% and nFeature < 3000. (**f**) Heatmap of top three genes expressed by each immune cell cluster. Data represent the mean ± SEM and statistical significance was determined by one-way ANOVA with Tukey's multiple comparison test for C and D. Asterisks represent p-values from multiple comparisons, with **** indicating a p-value of < 0.0001.

https://doi.org/10.1038/s41590-024-01859-0

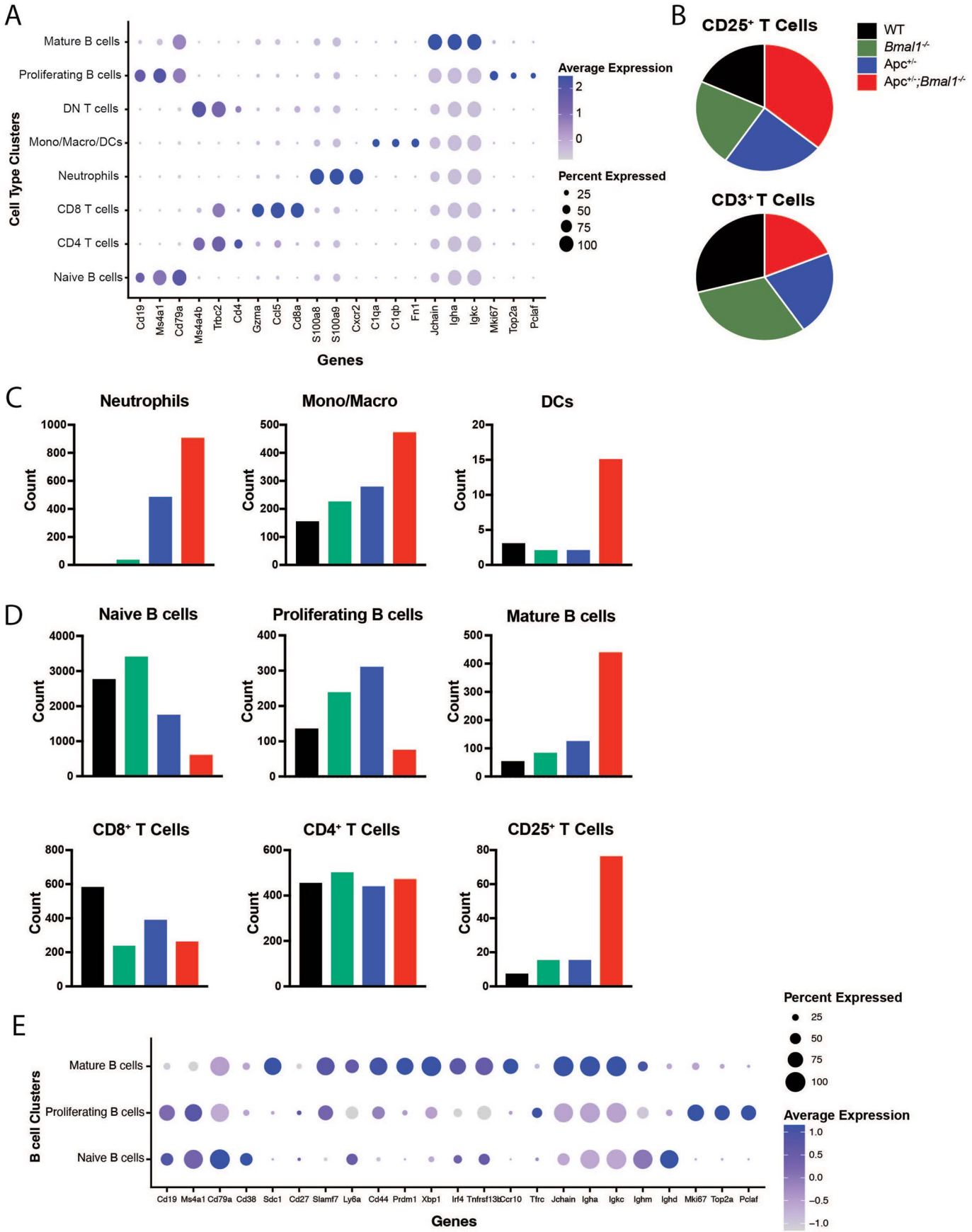

Extended Data Fig. 2 | See next page for caption.

https://doi.org/10.1038/s41590-024-01859-0

Extended Data Fig. 2 | scRNA-seq demonstrates that clock disruption alters the immune landscape. a) Dot-plot of gene expression by each immune cell cluster. (**b**) Pie chart of $CD25^+$ T cells and $CD3^+$ T cells from WT, *Bmal1*$^{-/-}$, *Apc*$^{+/-}$, and *Apc*$^{+/-}$;*Bmal1*$^{-/-}$ mice as determined by scRNA-seq. (**c**) Bar graph of immune cell count for neutrophils, monocytes/macrophages, and dendritic cells (DCs) from WT, *Bmal1*$^{-/-}$, *Apc*$^{+/-}$, and *Apc*$^{+/-}$;*Bmal1*$^{-/-}$ mice as determined by scRNA-seq. (**d**) Bar graph of immune cell count for naïve B cells, proliferating B cells, mature B cells, $CD8^+$ T cells, $CD4^+$ T cells, and $CD25^+$ T cells from WT, *Bmal1*$^{-/-}$, *Apc*$^{+/-}$, and *Apc*$^{+/-}$;*Bmal1*$^{-/-}$ mice as determined by scRNA-seq. (**e**) Dot-plot of gene expression for B cell clusters.

https://doi.org/10.1038/s41590-024-01859-0

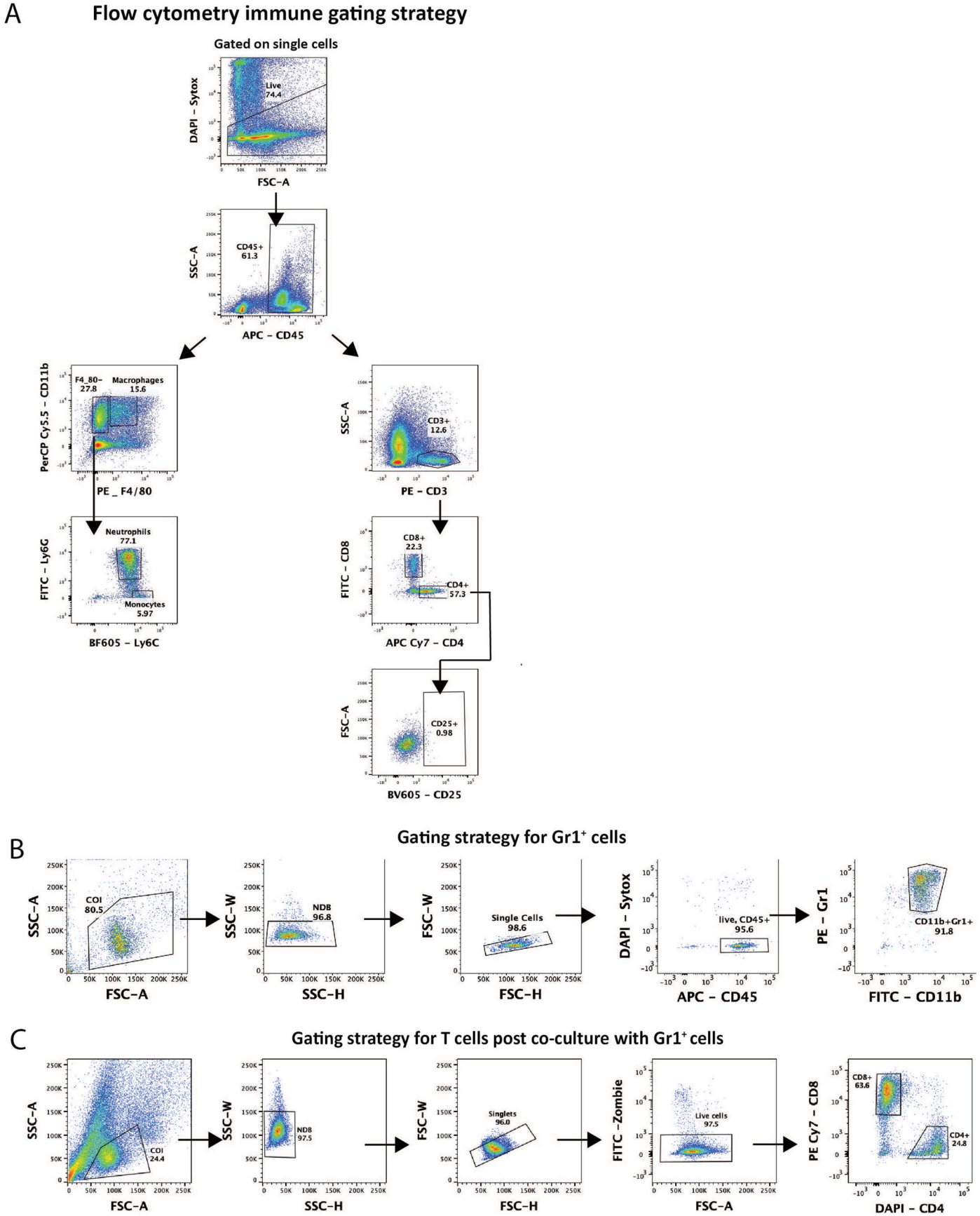

Extended Data Fig. 3 | Gating strategies for flow cytometric analysis of the immune landscape. (**a**) Gating strategy for flow cytometric analysis of immune cells. Markers include Sytox Blue, APC CD45, PerCP-Cy7 CD11b, PE F4/80, FITC Ly6G, BV605 Ly6C, PE CD3, FITC CD8, APC-Cy7 CD4, and BV605 CD25. (**b**) Gating strategy for sorting live, CD45$^+$CD11b$^+$Gr1$^+$ cells. Markers include Sytox Blue, APC CD45, PE Gr1, and FITC CD11b. (**c**) Gating strategy for T cells post co-culture with CD11b$^+$Gr1$^+$ cells. Markers include FITC Zombie, PE-Cy7 CD8, and DAPI CD4.

https://doi.org/10.1038/s41590-024-01859-0

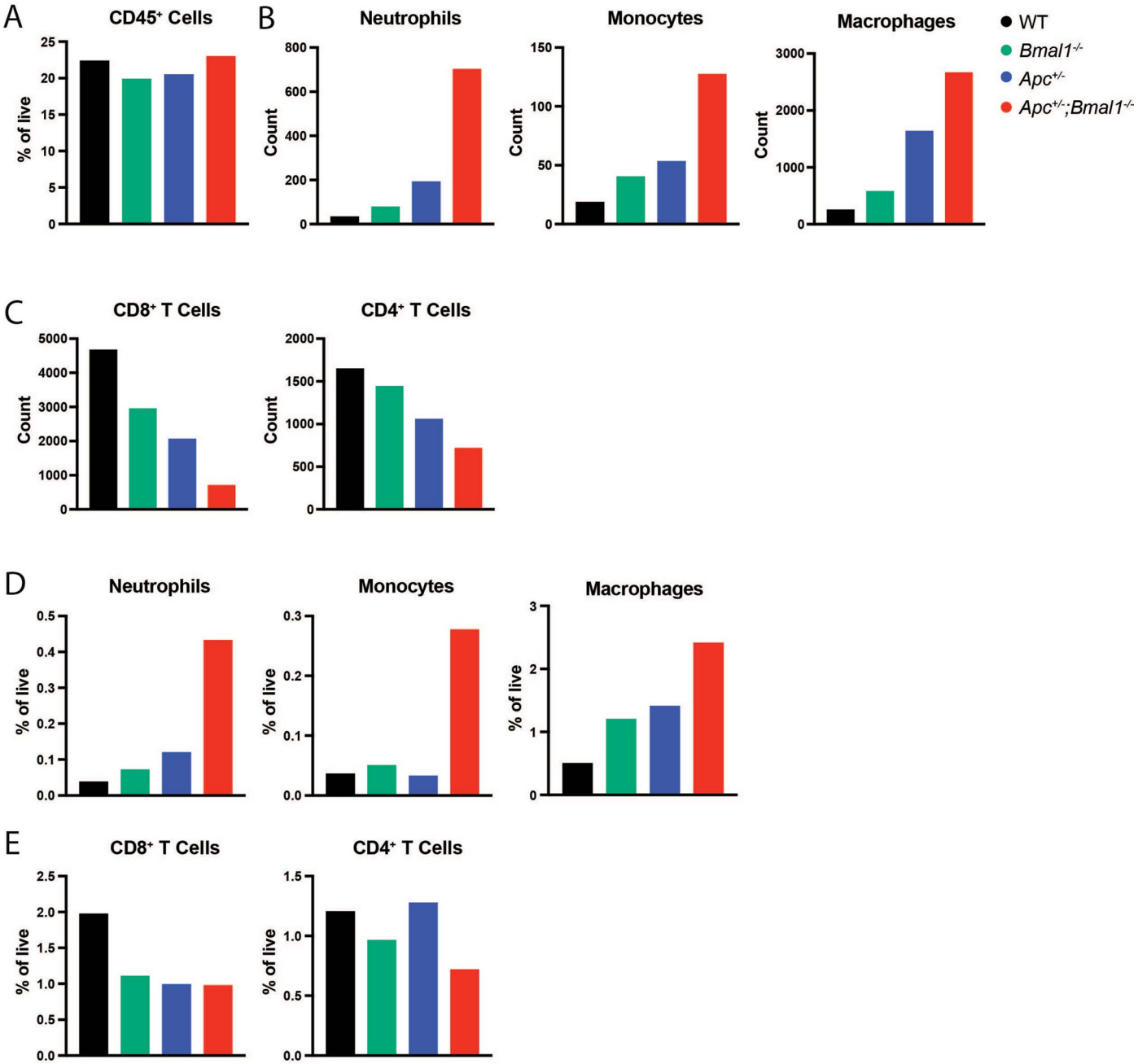

Extended Data Fig. 4 | Flow cytometry demonstrates that clock disruption alters immune proportions. (**a**) Bar graph of immune cells as percent of live cells from the intestine of WT, *Bmal1*$^{-/-}$, *Apc*$^{+/-}$, and *Apc*$^{+/-}$;*Bmal1*$^{-/-}$ mice sacrificed at ZT 4 and analyzed by flow cytometry (n = 7 mice/genotype). (**b**) Bar graph of immune cell counts for neutrophils, monocytes, and macrophages from WT, *Bmal1*$^{-/-}$, *Apc*$^{+/-}$, and *Apc*$^{+/-}$;*Bmal1*$^{-/-}$ mice sacrificed at ZT 4 and analyzed by flow cytometry (n = 7 mice/genotype). (**c**) Bar graph of immune cell counts for CD8^{+} T cells and CD4^{+} T cells from WT, *Bmal1*$^{-/-}$, *Apc*$^{+/-}$, and *Apc*$^{+/-}$;*Bmal1*$^{-/-}$ mice sacrificed at ZT 4 and analyzed by flow cytometry (n = 7 mice/genotype). (**d**) Bar graph of immune cells as percent of live for neutrophils, monocytes, and macrophages from WT, *Bmal1*$^{-/-}$, *Apc*$^{+/-}$, and *Apc*$^{+/-}$;*Bmal1*$^{-/-}$ sacrificed at ZT 4 and analyzed by flow cytometry (n = 7 mice/genotype). (**e**) Bar graph of immune cells as percent of live for CD4^{+} T cells and CD8^{+} T cells from WT, *Bmal1*$^{-/-}$, *Apc*$^{+/-}$, and *Apc*$^{+/-}$;*Bmal1*$^{-/-}$ mice sacrificed at ZT 4 and analyzed by flow cytometry (n = 7 mice/genotype).

https://doi.org/10.1038/s41590-024-01859-0

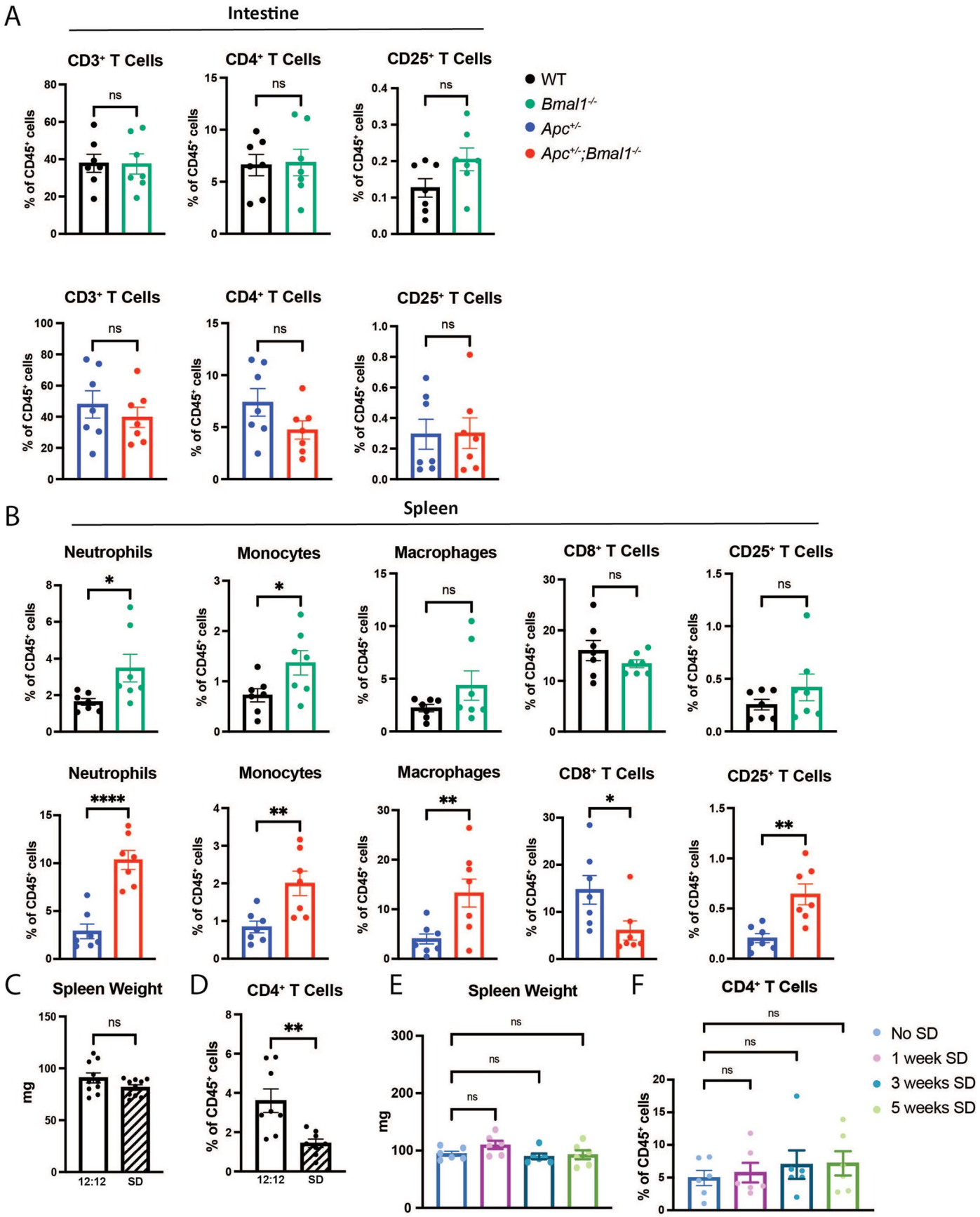

Extended Data Fig. 5 | See next page for caption.

https://doi.org/10.1038/s41590-024-01859-0

Extended Data Fig. 5 | Genetic and environmental clock disruption alter the immune landscape. (**a**) $CD3^+$ T cells, $CD4^+$ T cells, and $CD25^+$ T cells shown as percent of $CD45^+$ cells from the small intestine of WT, *Bmal1*$^{-/-}$, *Apc*$^{+/-}$, and *Apc*$^{+/-}$;*Bmal1*$^{-/-}$ mice sacrificed at ZT 4 and analyzed by flow cytometry (n = 7 mice/genotype). (**b**) Neutrophils, monocytes, macrophages, $CD8^+$ T cells, and $CD25^+$ T cells shown as percent of $CD45^+$ cells from the spleen of WT, *Bmal1*$^{-/-}$, *Apc*$^{+/-}$, and *Apc*$^{+/-}$;*Bmal1*$^{-/-}$ mice sacrificed at ZT 4 and analyzed by flow cytometry (n = 7 mice/genotype). (**c**) Spleen weight of WT mice subjected to 12:12 LD paradigm versus SD (n = 10 mice/genotype). (**d**) $CD4^+$ T cells shown as percent of $CD45^+$ cells from the small intestine of WT mice subjected to 12:12 LD versus SD. Mice were sacrificed at ZT 4 and analyzed by flow cytometry (n = 8 mice/genotype). (**e**) Spleen weight of WT mice subjected to 12:12 LD paradigm, 1 week SD, 3 weeks SD, and 5 weeks SD (n = 6 mice/genotype). (**f**) $CD4^+$ T cells shown as percent of $CD45^+$ cells from the small intestine of WT mice subjected to 12:12 LD paradigm, 1 week SD, 3 weeks SD, and 5 weeks SD. Mice were sacrificed at ZT 4 and analyzed by flow cytometry (n = 6 mice/genotype). Data represent the mean ± SEM and statistical significance was determined by two-tailed Mann-Whitney T-test for A–D, and one-way ANOVA with Tukey's multiple comparison test for E and F. Asterisks represent p-values from multiple comparisons, with * indicating a p-value of < 0.05, ** indicating a p-value of < 0.01, **** indicating a p-value of < 0.0001, and ns = not significant.

https://doi.org/10.1038/s41590-024-01859-0

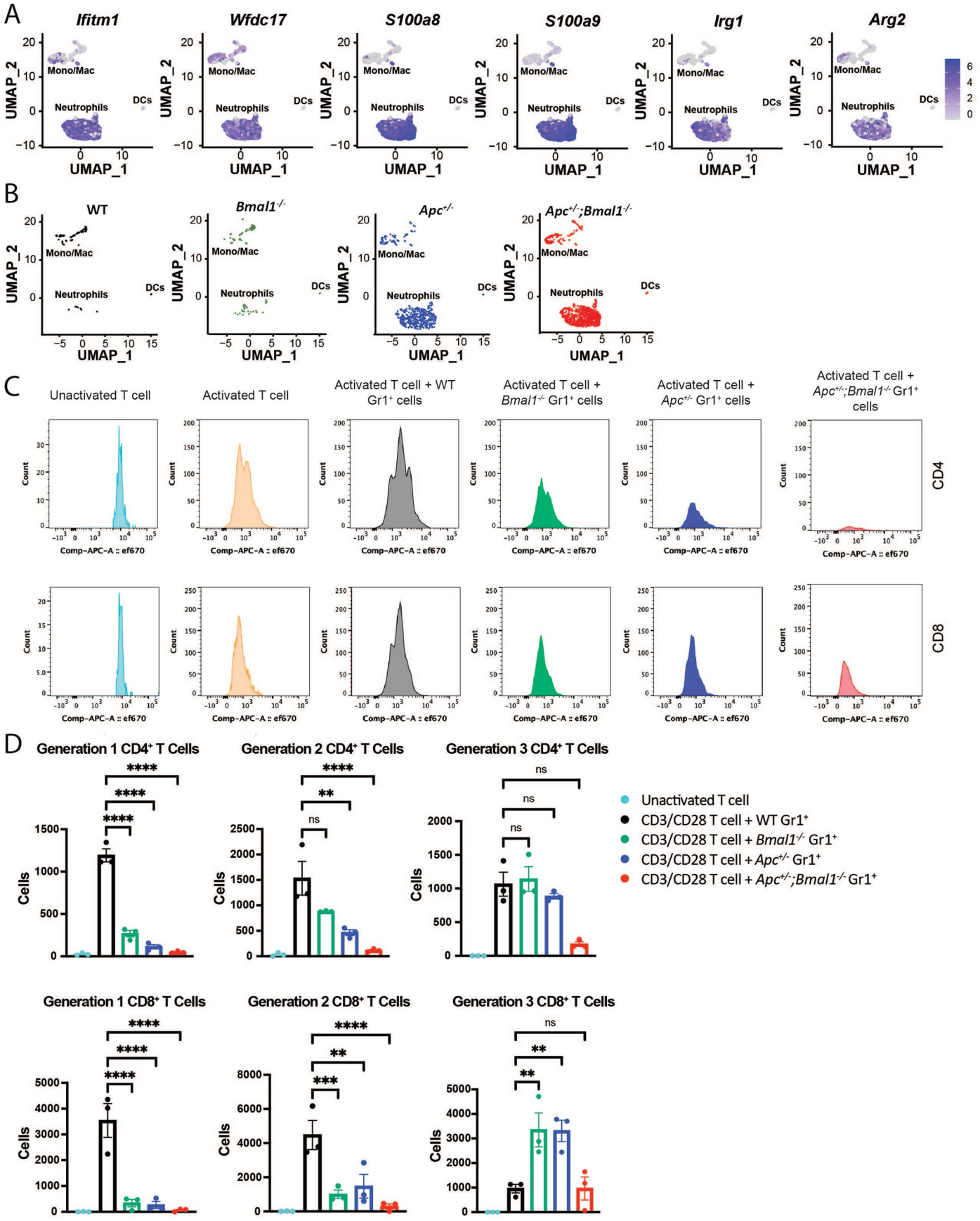

Extended Data Fig. 6 | See next page for caption.

https://doi.org/10.1038/s41590-024-01859-0

Extended Data Fig. 6 | scRNA-seq demonstrates that clock disruption promotes MDSC accumulation. (**a**) UMAP of the expression of *Ifitm1, Wfdc17, s100a8, s100a9, Irg1*, and *Arg2* by monocytes/macrophages, neutrophils, and DCs. (**b**) UMAP of monocytes/macrophages, neutrophils, and DCs in WT, *Bmal1*$^{-/-}$, *Apc*$^{+/-}$, and *Apc*$^{+/-}$;*Bmal1*$^{-/-}$ mice as determined by scRNA-seq. **c**) Histogram of CD4^{+} T cell and CD8^{+} T cell counts after co-culture with Gr1^{+} cells sorted from WT, *Bmal1*$^{-/-}$, *Apc*$^{+/-}$, and *Apc*$^{+/-}$;*Bmal1*$^{-/-}$ mice spleen. (**d**) Counts of generation 1, 2, and 3 CD4^{+} T cells and CD8^{+} T cells after co-culture with Gr1^{+} cells sorted from WT, *Bmal1*$^{-/-}$, *Apc*$^{+/-}$, and *Apc*$^{+/-}$;*Bmal1*$^{-/-}$ mice spleen (n = 3 mice/genotype). Data represent the mean ± SEM and statistical significance was determined by one-way ANOVA with Tukey's multiple comparison test for D. Asterisks represent p-values from multiple comparisons, with ** indicating a p-value of < 0.01, *** indicating a p-value of < 0.001, **** indicating a p-value of < 0.0001, and ns = not significant.

https://doi.org/10.1038/s41590-024-01859-0

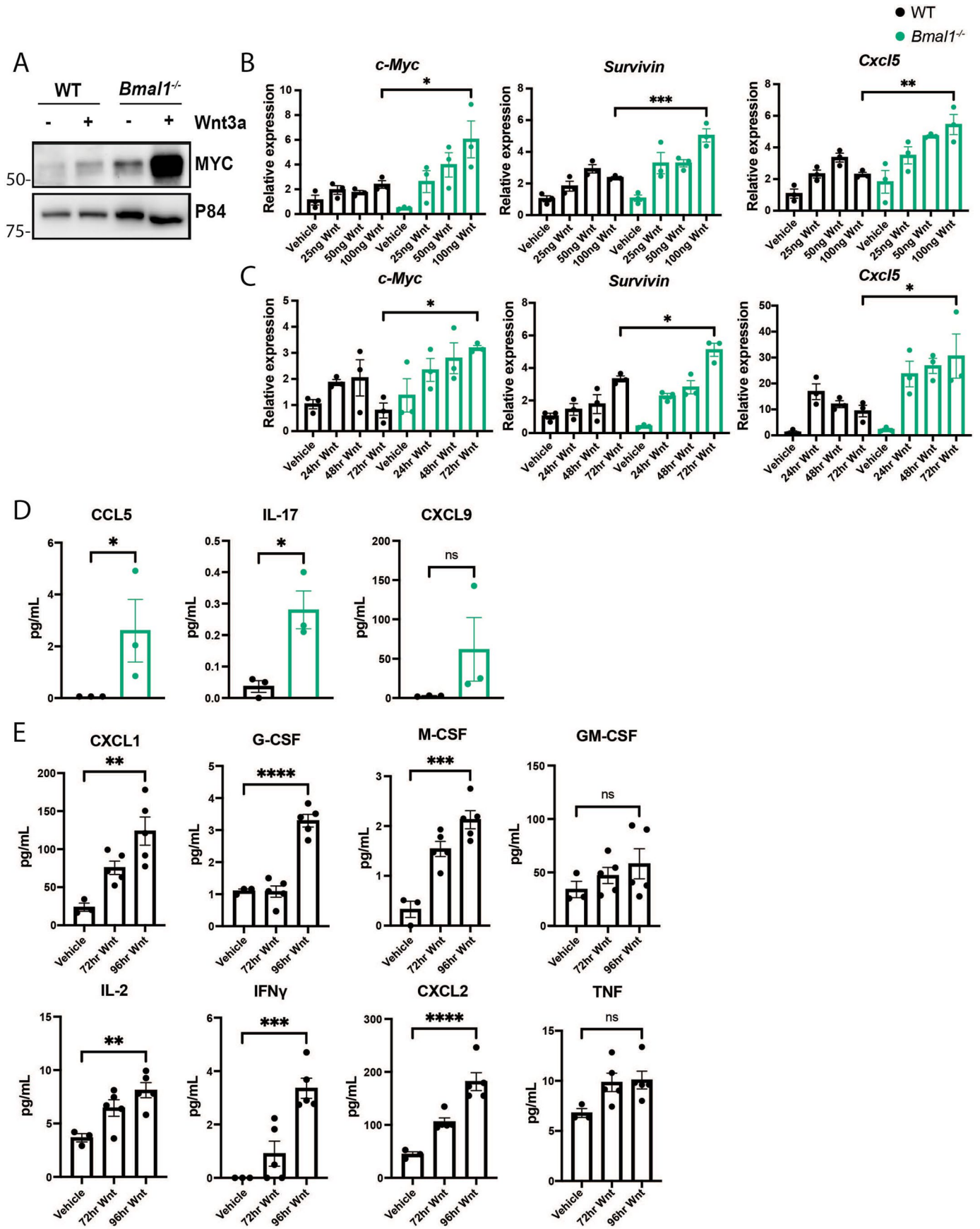

Extended Data Fig. 7 | See next page for caption.

https://doi.org/10.1038/s41590-024-01859-0

Extended Data Fig. 7 | Circadian clock disruption promotes an inflammatory response. (**a**) Western blot of MYC and p84 in WT and *Bmal1*$^{-/-}$ intestinal organoids untreated or treated with 100 ng/mL recombinant Wnt3a for 72 hours. (**b**) WT and *Bmal1*$^{-/-}$ intestinal organoids untreated or treated with 25, 50, or 100 ng/mL recombinant Wnt3a for 72 hours. Gene expression of *c-Myc, Survivin*, and *Cxcl5* was determined by qPCR (n = 3 independent organoid lines/genotype). (**c**) WT and *Bmal1*$^{-/-}$ intestinal organoids untreated or treated with 100 ng/mL recombinant Wnt3a for 24, 48, or 72 hours. Gene expression of *c-Myc, Survivin* and *Cxcl5* was determined by qPCR (n = 3 independent organoid lines/genotype). (**d**) Concentration of CCL5, IL-17, and CXCL9 in WT and *Bmal1*$^{-/-}$ intestinal monolayer lysate as determined by ELISA (n = 3 independent monolayer lines/genotype). (**e**) WT intestinal monolayers were left untreated or treated with 100 ng/mL recombinant Wnt3a for 96 hours (n = 3 untreated and 5 Wnt3a-treated independent monolayer lines/genotype). Concentration of CXCL1, G-CSF, M-CSF, GM-CSF, IL-2, IFNγ, CXCL2, and TNF in WT monolayer cell lysate was determined by ELISA. Data represent the mean ± SEM and statistical significance was determined by two-tailed Mann-Whitney T-test for D, and one-way ANOVA with Tukey's multiple comparison test for B-C, and E. Asterisks represent p-values from multiple comparisons, with * indicating a p-value of < 0.05, ** indicating a p-value of < 0.01, *** indicating a p-value of < 0.001, **** indicating a p-value of < 0.0001, and ns = not significant.

https://doi.org/10.1038/s41590-024-01859-0

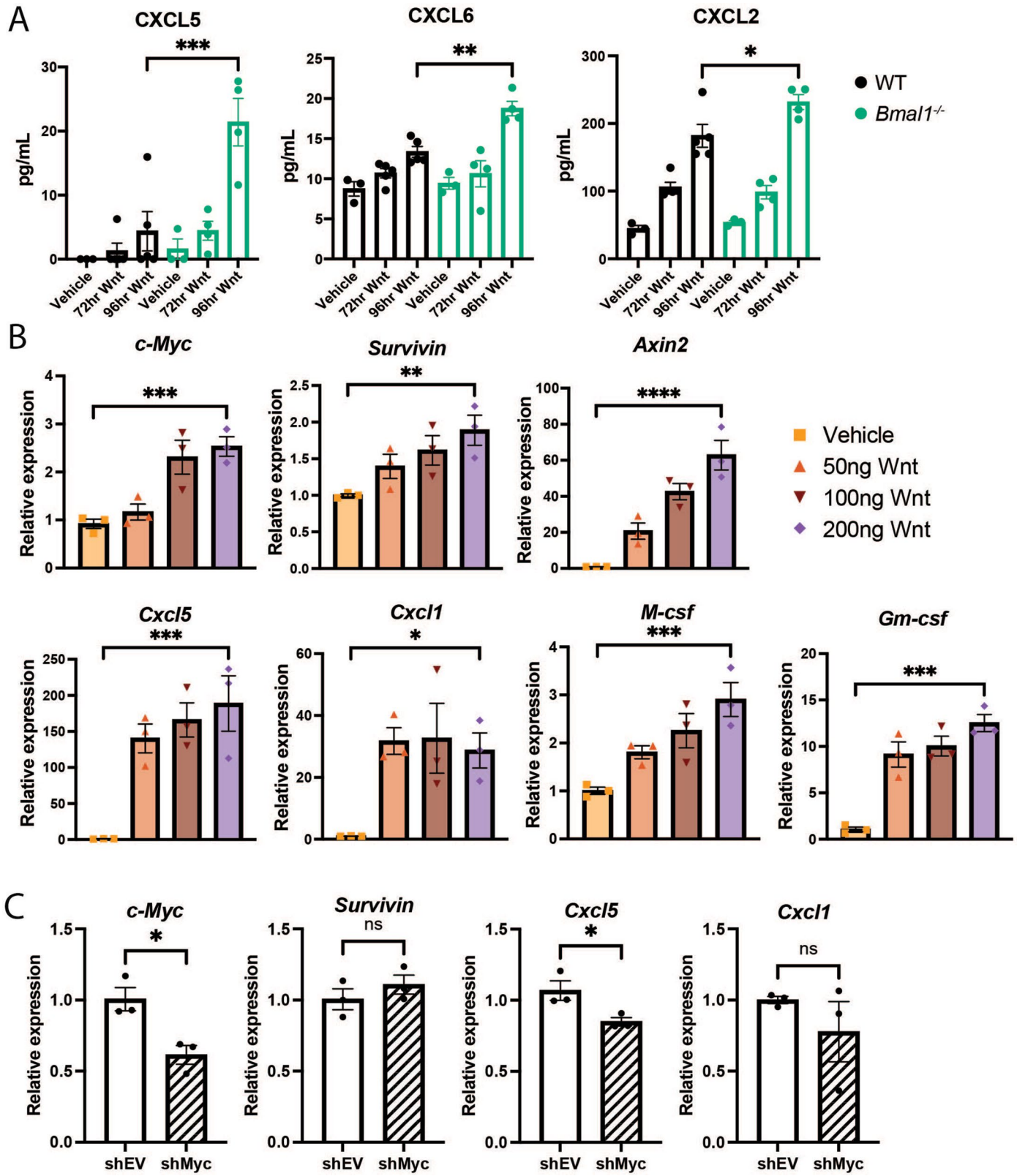

Extended Data Fig. 8 | Wnt signaling mediates the inflammatory response in the intestine. (**a**) WT and *Bmal1*$^{-/-}$ intestinal monolayers were left untreated or treated with 100 ng/mL recombinant Wnt3a for 96 hours (n = 3 untreated and 4 Wnt3a-treated independent monolayer lines/genotype). Concentration of CXCL5, CXCL6, and CXCL2 in intestinal monolayer lysate as determined by ELISA. (**b**) Expression of *c-Myc, Survivin, Axin2, Cxcl5, Cxcl1, M-csf*, and *Gm-csf* as determined by qPCR in mouse embryonic fibroblasts untreated or treated with 50, 100, or 200 ng/mL recombinant Wnt3a for 4 hours (n = 3 independent biological replicates/condition). (**c**) Expression of *c-Myc, Survivin, Cxcl5*, and *Cxcl1* as determined by qPCR using WT intestinal monolayers infected with shEV or shMyc (n = 3 independent monolayer lines). Data represent the mean ± SEM and statistical significance was determined by two-tailed Mann-Whitney T-test for C, and one-way ANOVA with Tukey's multiple comparison test for A-B. Asterisks represent p-values from multiple comparisons, with * indicating a p-value of < 0.05, ** indicating a p-value of < 0.01, *** indicating a p-value of < 0.001, **** indicating a p-value of < 0.0001, and ns = not significant.

https://doi.org/10.1038/s41590-024-01859-0

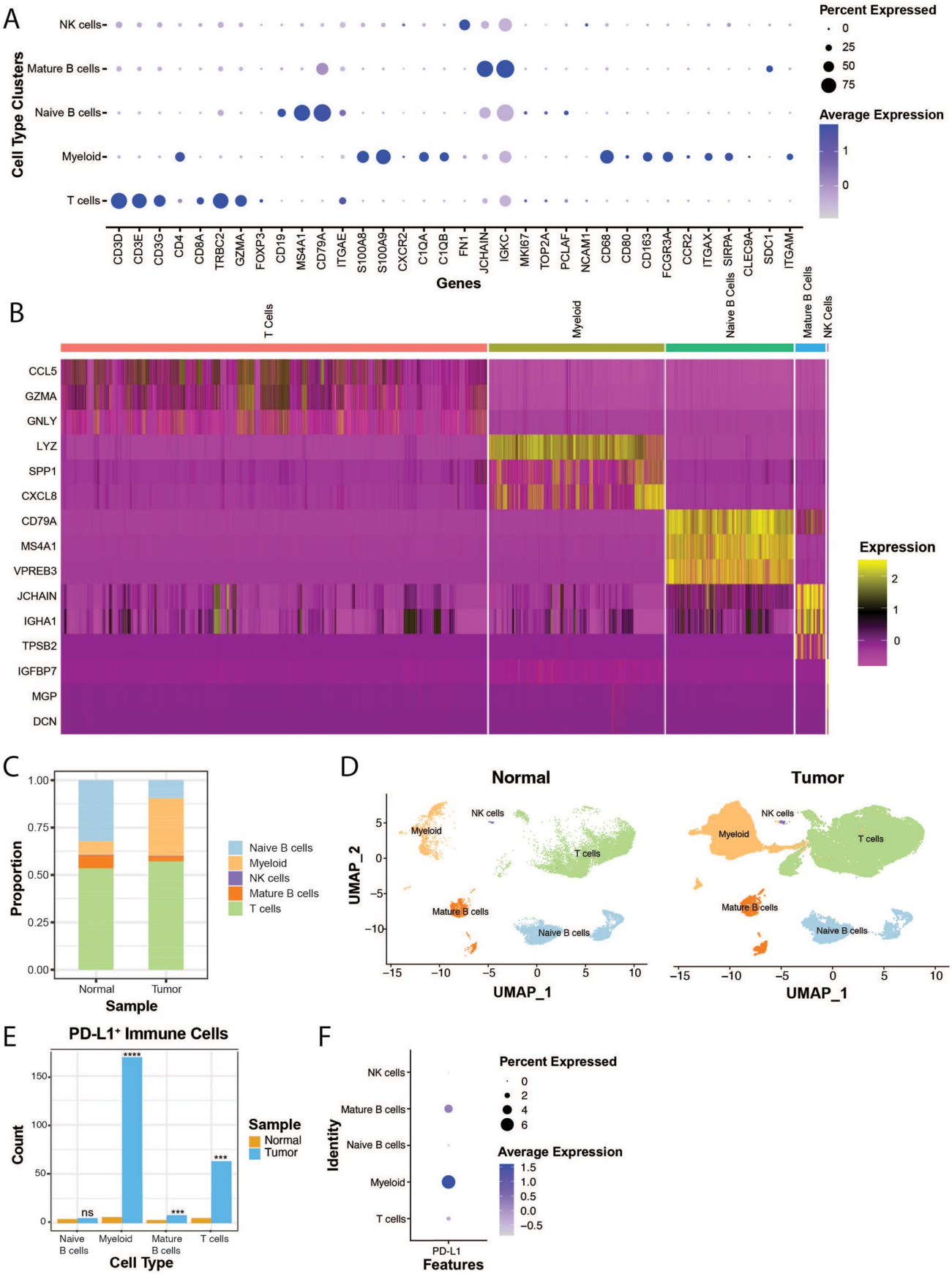

Extended Data Fig. 9 | See next page for caption.

https://doi.org/10.1038/s41590-024-01859-0

Extended Data Fig. 9 | scRNA-seq analysis of Gr1 and PD-L1 abundance in human CRC. Dataset from Pelka et al. (**a**) Dot-plot of gene expression by each immune cell cluster in matched normal colon and tumor samples. (**b**) Heatmap of cell types clustered by single-cell transcriptional analysis (n = 55,535 cells, n = 36 patients). (**c**) Stacked bar chart of human immune cell cluster composition determined using scRNA-seq dataset from Pelka et al. Data was based on 36 patients with matched normal colon and CRC tumor samples. (**d**) UMAP of human immune cell types clustered by single-cell transcriptional analysis broken down by normal and tumor (n = 36 patient samples/group). (**e**) Bar graph of cell counts expressing PD-L1 by human immune cell clusters in matched normal colon and CRC samples. (**f**) Dot-plot of PD-L1 expression by each human immune cell cluster in matched normal colon and CRC samples. Statistical significance was determined by one-way ANOVA with Tukey's multiple comparison test for E. Asterisks represent p-values from multiple comparisons, with *** indicating a p-value of < 0.001, **** indicating a p-value of < 0.0001, and ns = not significant.

https://doi.org/10.1038/s41590-024-01859-0

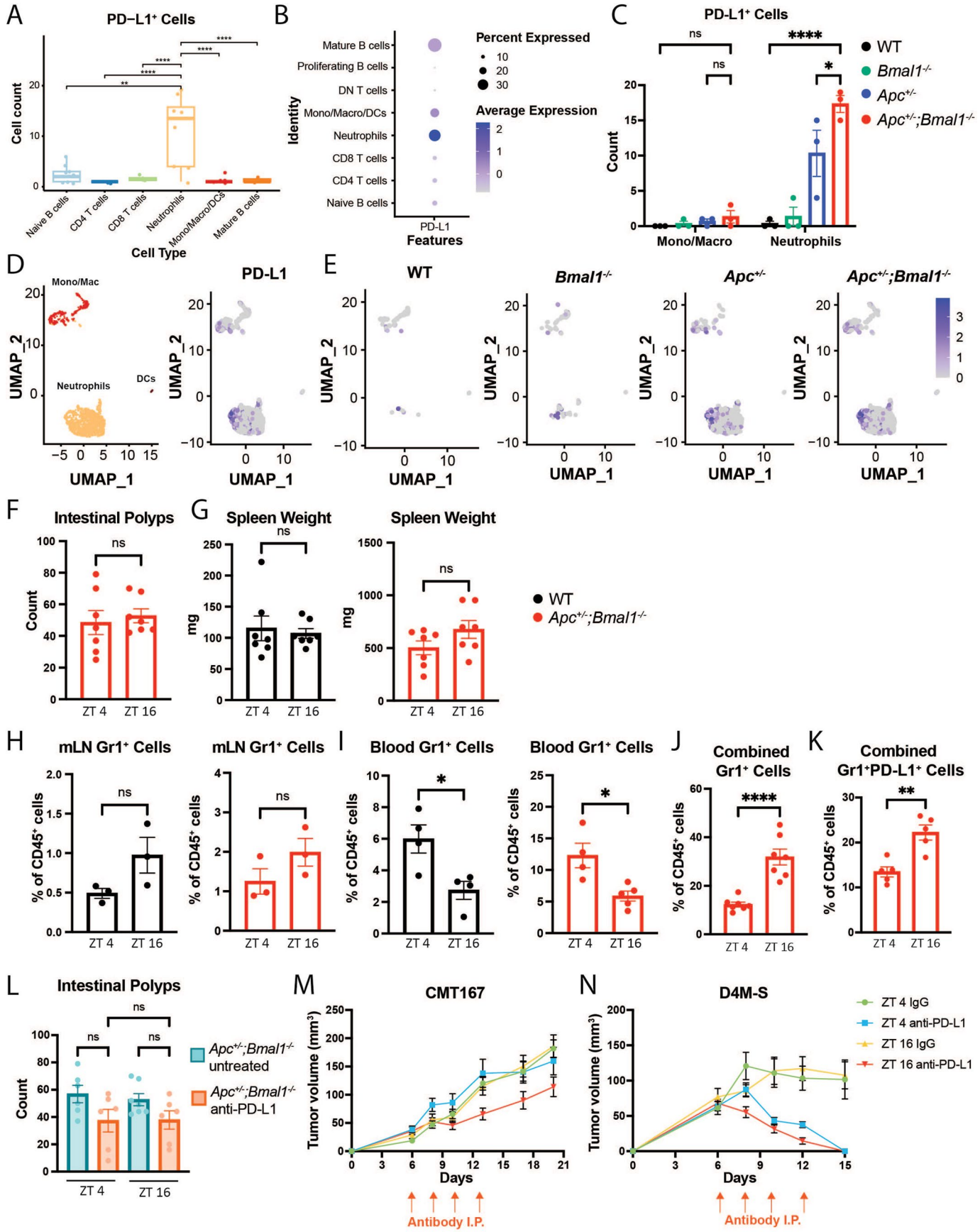

Extended Data Fig. 10 | See next page for caption.

https://doi.org/10.1038/s41590-024-01859-0

Extended Data Fig. 10 | The circadian clock regulates immunosuppression and anti-PD-L1 efficacy. (**a, b**) Box plot or dot-plot of PD-L1 expression by each immune cell cluster in mouse scRNA-seq data (n = 3 mice/genotype). Box plot center line represents the median, the boundaries represent IQR, and the whisker length represents 1.5 x IQR. (**c**) Bar graph of PD-L1 expression by monocyte/macrophage and neutrophil clusters in the intestine of WT, *Bmal1*$^{-/-}$, *Apc*$^{+/-}$, and *Apc*$^{+/-}$;*Bmal1*$^{-/-}$ mice determined by scRNA-seq (n = 3 mice/genotype). (**d-e**) UMAP of myeloid cell clusters and PD-L1 expression in the intestine of WT, *Bmal1*$^{-/-}$, *Apc*$^{+/-}$, and *Apc*$^{+/-}$;*Bmal1*$^{-/-}$ mice (n = 3 mice/genotype). (**f-g**) Small intestinal polyps and spleen weight in *Apc*$^{+/-}$;*Bmal1*$^{-/-}$ mice (n = 7 mice/group). (**h-i**) Mesenteric lymph node or blood Gr1^{+} cells as percent of CD45^{+} cells from WT and *Apc*$^{+/-}$;*Bmal1*$^{-/-}$ mice sacrificed at ZT 4 and ZT 16 and analyzed by flow cytometry (n = 3 mice/genotype for H, n = 4 mice/genotype for I). (**j**) Combined total Gr1^{+} cells from the small intestine and spleen as percent of CD45^{+} cells from *Apc*$^{+/-}$;*Bmal1*$^{-/-}$ mice sacrificed at ZT 4 and ZT 16 and analyzed by flow cytometry (n = 7 mice/group). (**k**) Combined total Gr1^{+}PD-L1^{+} cells from the small intestine and spleen as percent of CD45^{+} cells from *Apc*$^{+/-}$;*Bmal1*$^{-/-}$ mice. Animals were sacrificed at ZT 4 and ZT 16 and analyzed by flow cytometry (n = 5 mice/group). (**l**) Small intestinal polyp count from *Apc*$^{+/-}$;*Bmal1*$^{-/-}$ mice untreated or treated with anti-PD-L1 (n = 6 mice/group). (**m**) Tumor volume over time for WT mice after subcutaneous injection of CMT167 cells and treatment with IgG or anti-PD-L1 at ZT 4 or ZT 16 (n = 5 mice/group, 2 tumors/mouse). (**n**) Tumor volume over time for WT mice after subcutaneous injection of D4M-S cells and treatment with IgG or anti-PD-L1 at ZT 4 or ZT 16 (n = 5 mice/group, 2 tumors/mouse). Data represent the mean ± SEM and statistical significance was determined by two-tailed Mann-Whitney T-test for F-K, and by one-way ANOVA with Tukey's multiple comparison test for A, C, and L. Asterisks represent p-values from multiple comparisons, with * indicating a p-value of < 0.05, ** indicating a p-value of < 0.01, **** indicating a p-value of < 0.0001, and ns = not significant.

nature portfolio

Corresponding author(s): Dr. Selma Masri

Last updated by author(s): Apr 22, 2024

Reporting Summary

Nature Portfolio wishes to improve the reproducibility of the work that we publish. This form provides structure for consistency and transparency in reporting. For further information on Nature Portfolio policies, see our Editorial Policies and the Editorial Policy Checklist.

Statistics

For all statistical analyses, confirm that the following items are present in the figure legend, table legend, main text, or Methods section.

n/a	Confirmed
☐	☒ The exact sample size (*n*) for each experimental group/condition, given as a discrete number and unit of measurement
☐	☒ A statement on whether measurements were taken from distinct samples or whether the same sample was measured repeatedly
☐	☒ The statistical test(s) used AND whether they are one- or two-sided *Only common tests should be described solely by name; describe more complex techniques in the Methods section.*
☐	☒ A description of all covariates tested
☐	☒ A description of any assumptions or corrections, such as tests of normality and adjustment for multiple comparisons
☐	☒ A full description of the statistical parameters including central tendency (e.g. means) or other basic estimates (e.g. regression coefficient) AND variation (e.g. standard deviation) or associated estimates of uncertainty (e.g. confidence intervals)
☐	☒ For null hypothesis testing, the test statistic (e.g. *F*, *t*, *r*) with confidence intervals, effect sizes, degrees of freedom and *P* value noted *Give P values as exact values whenever suitable.*
☒	☐ For Bayesian analysis, information on the choice of priors and Markov chain Monte Carlo settings
☒	☐ For hierarchical and complex designs, identification of the appropriate level for tests and full reporting of outcomes
☒	☐ Estimates of effect sizes (e.g. Cohen's *d*, Pearson's *r*), indicating how they were calculated

Our web collection on statistics for biologists contains articles on many of the points above.

Software and code

Policy information about availability of computer code

Data collection	Library generation was performed following the Chromium NextGEM Single Cell v3.1 Cell Multiplexing Reagents Kits User Guide: CG000388Rev B. Multiplexed, single cell gene expression libraries were sequenced on the Illumina HiSeq. Alignment of 3′ end counting libraries from scRNAseq analyses was completed utilizing 10× Genomics cellranger-6.1.2. Each library was aligned to an indexed mm10 genome using Cell Ranger Count.
Data analysis	All scRNA-seq analysis was performed in R (v4.2.1) using Rstudio (v 2023.03.1 Build 446) and the Seurat v4 package. Cellranger outputs were loaded onto R. Packages used in the analysis of scRNA-seq data include ggplot2 (v 3.5.0) and ggpubr (v 0.6.0).

For manuscripts utilizing custom algorithms or software that are central to the research but not yet described in published literature, software must be made available to editors and reviewers. We strongly encourage code deposition in a community repository (e.g. GitHub). See the Nature Portfolio guidelines for submitting code & software for further information.

Data

Policy information about availability of data

All manuscripts must include a data availability statement. This statement should provide the following information, where applicable:

- Accession codes, unique identifiers, or web links for publicly available datasets
- A description of any restrictions on data availability
- For clinical datasets or third party data, please ensure that the statement adheres to our policy

The single cell RNA-sequencing data have been deposited at the NCBI Gene Expression Omnibus (GEO) under the GEO accession number GSE262267 and at the Sequence Read Archive (SRA) under SRA accession number PRJNA1003452.

Research involving human participants, their data, or biological material

Policy information about studies with human participants or human data. See also policy information about sex, gender (identity/presentation), and sexual orientation and race, ethnicity and racism.

Reporting on sex and gender	Human data were obtained from Pelka et al. Data were obtained from 30 males and 32 females and findings in this study applied to both males and females.
Reporting on race, ethnicity, or other socially relevant groupings	Race and ethnicity were not included. All tumor samples included also had a matched normal sample so relevant groupings should be controlled for.
Population characteristics	All tumor samples included a matched normal sample from the same patient.
Recruitment	See Pelka et al.
Ethics oversight	See Pelka et al.

Note that full information on the approval of the study protocol must also be provided in the manuscript.

Field-specific reporting

Please select the one below that is the best fit for your research. If you are not sure, read the appropriate sections before making your selection.

☒ Life sciences ☐ Behavioural & social sciences ☐ Ecological, evolutionary & environmental sciences

For a reference copy of the document with all sections, see nature.com/documents/nr-reporting-summary-flat.pdf

Life sciences study design

All studies must disclose on these points even when the disclosure is negative.

Sample size	Sample sizes were determined using the proper power analysis test for either t-test or one-way ANOVA and a confidence of 90%.
Data exclusions	For flow cytometry data, data were excluded if the percent of live cells was below 50%.
Replication	All experiments were performed successfully a minimum of three separate times to confirm reproducibility.
Randomization	For ZT4 versus ZT16 and anti-PD-L1 experiments, mice were age and gender matched prior to separation into groups.
Blinding	Experiments were not performed blinded.

Reporting for specific materials, systems and methods

We require information from authors about some types of materials, experimental systems and methods used in many studies. Here, indicate whether each material, system or method listed is relevant to your study. If you are not sure if a list item applies to your research, read the appropriate section before selecting a response.

Materials & experimental systems

n/a	Involved in the study
☐	☒ Antibodies
☐	☒ Eukaryotic cell lines
☒	☐ Palaeontology and archaeology
☐	☒ Animals and other organisms
☒	☐ Clinical data
☒	☐ Dual use research of concern
☒	☐ Plants

Methods

n/a	Involved in the study
☒	☐ ChIP-seq
☐	☒ Flow cytometry
☒	☐ MRI-based neuroimaging

Antibodies

Antibodies used

1:200 CD45 [BioLegend, 103112, clone 30-F11 (APC)]
1:50 CD11b [BioLegend, 101228 , clone M1/70 (PerCP/cyanine5.5), 101205, clone M1/70 (FITC) or 101225, clone M1/70 (APC/Cy7)]
1:100 Gr1 [BioLegend, 108439, clone RB6-8C5 (BV605) or 108407, clone RB6-8C5 (PE)]
1:100 F4/80 [Biolegend, 123110, clone BM8 (PE)]
1:100 Ly6C [BioLegend, 128035, clone HK1.4 (BV605)]
1:100 Ly6G [BioLegend, 127606, clone 1A8 (FITC)]
1:100 CD3 [TONBO Biosciences, 50-0032, clone 17A2 (PE)]
1:160 CD4 [Life Technologies, 46-0042-82, clone RM4-5 (eFluor710)]
1:100 CD8 [RndSystems, FAB116G, clone 53-6.7 (AlexaFluor488)]
1:100 CD25 [BioLegend, 102037, clone PC61 (BV650)]
1:200 PD-L1 [Tonbo Biosciences, 50-1243, clone B7-H1 (PE)]
1:1000 Sytox Blue dye (Life Technologies, S34857) was added to stained cells to assay for viability.

Validation

All antibodies used were validated by the manufacturer including confirmed reactivity against mouse tissues and quality control testing by immunofluorescent staining with flow cytometric analysis.

Eukaryotic cell lines

Policy information about cell lines and Sex and Gender in Research

Cell line source(s)

The following cell lines were used in the study: human embryonic kidney cells (Hek293)mouse embryonic fibroblasts (MEFs), mouse MC38 colon cancer cells, mouse CMT167 lung cancer cells, and mouse D4M-S melanoma cells.

Authentication

All cell lines used were authenticated by the manufacturer using short tandem repeat (STR) profiling.

Mycoplasma contamination

All cell lines used in the study were confirmed to be negative for mycoplasma contamination.

Commonly misidentified lines
(See ICLAC register)

No commonly misidentified cell lines were used in this study.

Animals and other research organisms

Policy information about studies involving animals; ARRIVE guidelines recommended for reporting animal research, and Sex and Gender in Research

Laboratory animals

All mice were are from the C57BL/6 background. Apc mice that harbor a heterozygous floxed allele of exons 1 to 15 (Apc+/Δex1–15) 83 were crossed with Bmal1 conditional mice that carry homozygous floxed alleles of exon 8 (Bmal1fl/fl) 84. Intestine-specific targeting of epithelial cells was achieved by crossing these conditional mice with Villin-Cre animals to create Apc+/Δex1–15;Bmal1fl/fl;Villin-Cre mice. Mice were purchased from the Jackson Laboratory (Bar Harbor, ME). Mice were sacrificed for experiments at 9-10 months of age except for the WT SD experiment where mice were sacrificed at 4 months of age.

All experiments were performed in accordance with the Institutional Animal Care and Use Committee (IACUC) guidelines at the University of California, Irvine. Animals were housed on a standard 12-hour light/12-hour dark paradigm, with temperatures of 65-75 °F, humidity 40-60%, and fed ad libitum.

Wild animals

This study did not involve wild animals.

Reporting on sex

All experiments were performed with mice of both sexes other than the subcutaneous models. For the subcutaneous mouse experiments, mice of only one gender were used in order to prevent rejection of the cancer cells.

Field-collected samples

This study did not involve samples collected from the field.

Ethics oversight

All experiments were performed in accordance with the Institutional Animal Care and Use Committee (IACUC) guidelines at the University of California, Irvine.

Note that full information on the approval of the study protocol must also be provided in the manuscript.

Plants

Seed stocks

Report on the source of all seed stocks or other plant material used. If applicable, state the seed stock centre and catalogue number. If plant specimens were collected from the field, describe the collection location, date and sampling procedures.

Novel plant genotypes

Describe the methods by which all novel plant genotypes were produced. This includes those generated by transgenic approaches, gene editing, chemical/radiation-based mutagenesis and hybridization. For transgenic lines, describe the transformation method, the number of independent lines analyzed and the generation upon which experiments were performed. For gene-edited lines, describe the editor used, the endogenous sequence targeted for editing, the targeting guide RNA sequence (if applicable) and how the editor was applied.

Authentication

Describe any authentication procedures for each seed stock used or novel genotype generated. Describe any experiments used to assess the effect of a mutation and, where applicable, how potential secondary effects (e.g. second site T-DNA insertions, mosiacism, off-target gene editing) were examined.

Flow Cytometry

Plots

Confirm that:

☒ The axis labels state the marker and fluorochrome used (e.g. CD4-FITC).

☒ The axis scales are clearly visible. Include numbers along axes only for bottom left plot of group (a 'group' is an analysis of identical markers).

☒ All plots are contour plots with outliers or pseudocolor plots.

☒ A numerical value for number of cells or percentage (with statistics) is provided.

Methodology

Sample preparation

All samples were collected from mice.

Spleen tissue collection and cell isolation
Animals were sacrificed at the ZT indicated in the legend, spleens were quickly excised, pushed through a 70-µm cell strainer to create a cell suspension of splenocytes and washed with RPMI. Cells were centrifuged at 500g at 4°C for 10 min and then incubated for 1 min in 5 mL RBC lysis buffer at RT. Cells were quenched with 10 mL serum-free PBS and pelleted by centrifugation at 500g at 4°C for 5 min. Cells were resuspended in 5 mL FACS buffer (1xPBS, 10% FBS), and total remaining live cells were counted by Countess™ II and processed for downstream FACS analysis.

Small intestine tissue collection and cell isolation
Tissue samples were harvested from mice at the ZT indicated in the legend, flushed, and cut longitudinally. Tissues were placed in RPMI media containing 1% FBS, 18 µg/mL DNase1 (Sigma-Aldrich, 04536282001) and 0.6 mg/mL Collagenase type P (Roche, #11249002001) and were digested at 37°C on a shaker for 30 min. Cells were filtered through a 70-µm cell strainer, washed with PBS containing 1M HEPES and 2% FBS. Samples were centrifuged to pellet cells, which were then resuspended in RPMI medium, filtered through a 40-µm cell strainer, and washed with PBS containing 1M HEPES and 2% FBS. Cells were centrifuged at 500g at 4°C for 5 min and then incubated for 1 min in 1 mL RBC lysis buffer at RT. Cells were quenched with 10 mL serum-free PBS and centrifuged at 500g at 4°C for 5 min. Cells were resuspended in 5 mL FACS buffer (1xPBS, 10% FBS), and total remaining live cells were counted by Countess™ II and processed for FACS analysis.

Lymph node collection and cell isolation
The mesenteric, dLN was collected at the ZT indicated in the legend and teased open with a 23G needle before being placed in digestion solution containing 1 mg/mL Collagenase D and A. After incubating at 37 °C on a shaker for 20 min, cells were filtered through a 70-µm cell strainer and washed with PBS. Samples were centrifuged to pellet cells, which were then resuspended in 1 mL FACS buffer (1xPBS, 10% FBS), and total remaining live cells were counted by Countess™ II and processed for FACS analysis.

Blood collection and cell isolation
Blood was collected at the ZT indicated in the legend by cardiac puncture and 0.5M EDTA was added to blood at a ratio of 1:10. Blood was incubated for 5 min in 2 mL RBC lysis buffer at RT. Cells were quenched with 10 mL serum-free PBS and centrifuged at 500g at 4°C for 5 min. Red blood cell lysis was repeated again and then cells were resuspended in 1 mL FACS buffer (1xPBS, 10% FBS), and total remaining live cells were counted by Countess™ II and processed for FACS analysis.

Fluorescence-Activated Cell Sorting (FACS)
Tissue samples were harvested from mice at the ZT indicated in the legend and mechanically dissociated to generate single cell suspensions as described above. Cells were blocked with anti-mouse FcγR (CD16/CD32) (BioLegend, 101301) on ice for 5 min. Cells were then centrifuged at 400g for 3 min at 4°C and washed once with FACS buffer (1xPBS with 10%FBS). Cells were incubated for 30 min at 4°C with pre-conjugated fluorescent labeled antibodies. Sytox Blue dye (Life Technologies, S34857) was added to stained cells to assay for viability.

Instrument

Cells were sorted by BD FACSAria™ Fusion

Software	Data was analyzed using FlowJo software, v10.0.7 (Tree Star, Inc).
Cell population abundance	*Describe the abundance of the relevant cell populations within post-sort fractions, providing details on the purity of the samples and how it was determined.*
Gating strategy	For all flow cytometry experiments, SSC-A and FSC-A were used to gate the cell of interest and then SSC-W and SSC-H as well as FSC-W and FSC-H were used to discard doublets. Live cells were gated using DAPI Sytox blue before gating based on other fluorophores. All experiments included single stain controls and gates were determined using fluorescence minus one (FMO) controls.

☒ Tick this box to confirm that a figure exemplifying the gating strategy is provided in the Supplementary Information.